Cell

Metabolic modeling of single Th17 cells reveals regulators of autoimmunity

Graphical Abstract

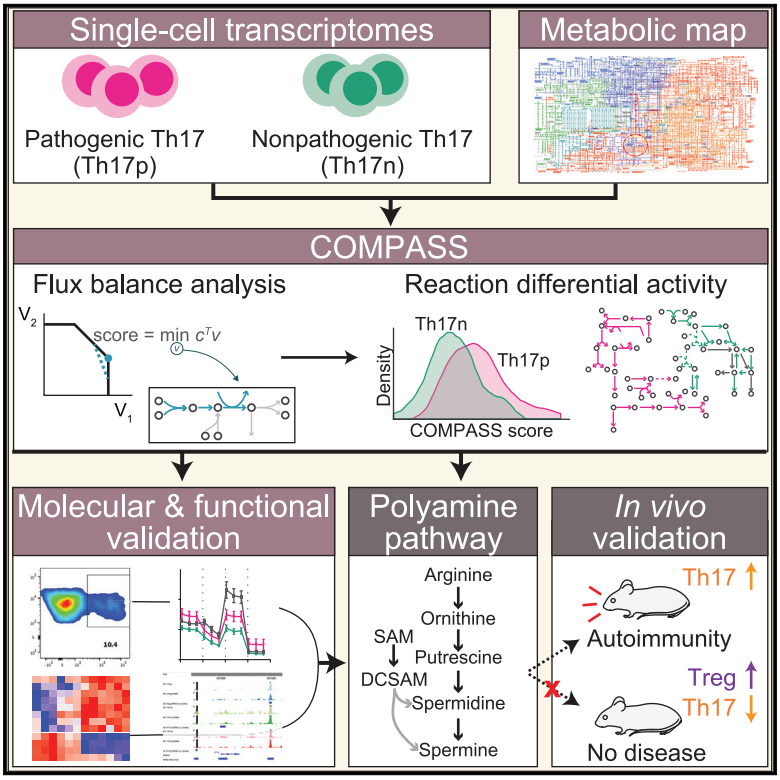

Highlights

- Compass enables studying cellular metabolism based on single-cell transcriptomes
- Compass links the pathogenic potential of Th17 cells with their metabolic programs
- Th17 pathogenicity is associated with a switch between glycolysis and beta oxidation
- The polyamine pathway is required for Th17 induction and restriction of a Treg profile

Authors

Allon Wagner, Chao Wang, Johannes Fessler, ..., Aviv Regev, Vijay K. Kuchroo, Nir Yosef

Correspondence

chao.wang@sri.utoronto.ca (C.W.), vkuchroo@evergrande.hms.harvard.edu (V.K.K.), niryosef@berkeley.edu (N.Y.)

In brief

Compass is an algorithm that derives information on cellular metabolic states from single-cell transcriptomic data. When applied to Th17 cells, it provides insights into how targeting the polyamine pathway can modulate encephalitis-associated T cells and attenuate autoimmune disease associated with the CNS.

Wagner et al., 2021, Cell *184*, 4168–4185
August 5, 2021 © 2021 Elsevier Inc.
https://doi.org/10.1016/j.cell.2021.05.045

CellPress

CellPress

Cell

Article

Metabolic modeling of single Th17 cells reveals regulators of autoimmunity

Allon Wagner,[1,2,18] Chao Wang,[3,4,5,6,18,*] Johannes Fessler,[4] David DeTomaso,[2] Julian Avila-Pacheco,[3] James Kaminski,[2] Sarah Zaghouani,[4] Elena Christian,[3] Pratiksha Thakore,[3] Brandon Schellhaass,[1] Elliot Akama-Garren,[4] Kerry Pierce,[3] Vasundhara Singh,[3] Noga Ron-Harel,[7,8] Vivian Paraskevi Douglas,[9] Lloyd Bod,[4] Alexandra Schnell,[4] Daniel Puleston,[10] Raymond A. Sobel,[11] Marcia Haigis,[7] Erika L. Pearce,[10] Manoocher Soleimani,[12] Clary Clish,[3] Aviv Regev,[3,13,14,17] Vijay K. Kuchroo,[3,4,19,*] and Nir Yosef[1,2,15,16,18,19,20,*]

[1]Department of Electrical Engineering and Computer Science, University of California, Berkeley, Berkeley, CA 94720, USA
[2]Center for Computational Biology, University of California, Berkeley, Berkeley, CA 94720, USA
[3]Broad Institute of MIT and Harvard, Cambridge, MA 02142, USA
[4]Evergrande Center for Immunologic Diseases, Harvard Medical School and Brigham and Women's Hospital, Boston, MA 02115, USA
[5]Biological Sciences Platform, Sunnybrook Research Institute, Toronto, ON M4N 3M5, Canada
[6]Department of Immunology, University of Toronto, Toronto, ON M5S 1A8, Canada
[7]Department of Cell Biology, Blavatnik Institute, Harvard Medical School, Boston, MA 02115, USA
[8]Department of Biology, Technion, Israel Institute of Technology, Haifa 3200003, Israel
[9]Massachusetts Eye and Ear, Department of Ophthalmology, Harvard Medical School, Boston, MA 02114, USA
[10]Max Planck Institute of Immunobiology and Epigenetics, 79108 Freiburg, Germany
[11]Palo Alto Veteran's Administration Health Care System and Department of Pathology, Stanford University School of Medicine, Stanford, CA 94305, USA
[12]Department of Medicine, University of New Mexico Health Sciences Center, Albuquerque, NM 87121, USA
[13]Koch Institute for Integrative Cancer Research, Massachusetts Institute of Technology, Cambridge, MA 02139, USA
[14]Department of Biology, Howard Hughes Medical Institute, Massachusetts Institute of Technology, Cambridge, MA 02140, USA
[15]Chan-Zuckerberg Biohub, San Francisco, CA 94158, USA
[16]Ragon Institute of MGH, MIT, and Harvard, Cambridge, MA 02139, USA
[17]Present address: Genentech, 1 DNA Way, South San Francisco, CA 94080, USA
[18]These authors contributed equally
[19]These authors contributed equally
[20]Lead contact
*Correspondence: chao.wang@sri.utoronto.ca (C.W.), vkuchroo@evergrande.hms.harvard.edu (V.K.K.), niryosef@berkeley.edu (N.Y.)
https://doi.org/10.1016/j.cell.2021.05.045

SUMMARY

Metabolism is a major regulator of immune cell function, but it remains difficult to study the metabolic status of individual cells. Here, we present Compass, an algorithm to characterize cellular metabolic states based on single-cell RNA sequencing and flux balance analysis. We applied Compass to associate metabolic states with T helper 17 (Th17) functional variability (pathogenic potential) and recovered a metabolic switch between glycolysis and fatty acid oxidation, akin to known Th17/regulatory T cell (Treg) differences, which we validated by metabolic assays. Compass also predicted that Th17 pathogenicity was associated with arginine and downstream polyamine metabolism. Indeed, polyamine-related enzyme expression was enhanced in pathogenic Th17 and suppressed in Treg cells. Chemical and genetic perturbation of polyamine metabolism inhibited Th17 cytokines, promoted Foxp3 expression, and remodeled the transcriptome and epigenome of Th17 cells toward a Treg-like state. *In vivo* perturbations of the polyamine pathway altered the phenotype of encephalitogenic T cells and attenuated tissue inflammation in CNS autoimmunity.

INTRODUCTION

Cellular metabolism regulates normal cell functions as well as the pathophysiology of multiple disease conditions. Recently, the study of metabolism in immune cells (immunometabolism) emerged as an active field of research and revealed metabolic regulation of inflammation in almost all contexts, including anti-viral immunity, autoimmunity, and anti-tumor response (Buck et al., 2017; Certo et al., 2021; Chapman et al., 2020; Diskin et al., 2021; Elia and Haigis, 2021; Geltink et al., 2018; Ho and Kaech, 2017; Hotamisligil, 2017; Jung et al., 2019; Makowski et al., 2020; O'Neill et al., 2016; Roy et al., 2021; Russell et al., 2019; Varanasi et al., 2020).

Due to the scale and complexity of the metabolic network, a metabolic perturbation can create cascading effects and alter a seemingly distant part of the network or cut across traditional pathway definitions. Therefore, computational tools are needed to contextualize observations on specific reactions or enzymes into a systems-level understanding of metabolism and its dysregulation in disease. One successful framework is flux balance analysis (FBA), which translates curated knowledge on the network's topology and stoichiometry into mathematical objects used for *in silico* predictions on metabolic fluxes (Lewis et al., 2012; O'Brien et al., 2015; Orth et al., 2010; Palsson, 2015). FBA methods proved particularly useful when contextualized with functional genomic data (Bordbar et al., 2014), usually gene expression of bulk cell populations. The advent of single-cell RNA sequencing (scRNA-seq) now offers an opportunity to harness FBA to study the metabolic heterogeneity of single cells.

We and others have studied transcriptional and functional diversity among T helper 17 (Th17) cells (Gaublomme et al., 2015; Wang et al., 2015) and Foxp3$^+$ regulatory T cells (Tregs) (Miragaia et al., 2019). Th17 and Treg cells share lineage signals, and their balance shapes the outcome of tissue inflammation (Eisenstein and Williams, 2009; Omenetti and Pizarro, 2015). Although transforming growth factor β1 (TGF-β1) alone induces Foxp3$^+$ Tregs *in vitro*, a combination of TGF-β1 and interleukin (IL)-6 induce Th17 cells *in vitro* and *in vivo* (Bettelli et al., 2006; Mangan et al., 2006; McGeachy and Cua, 2008; Veldhoen et al., 2006).

On top of the Th17/Treg balance, there exists functional diversity within the Th17 compartment. Th17 cells may induce disease but they also protect mucosal tissues by promoting tissue homeostasis, maintaining barrier function, and restraining opportunistic microbiota (Bettelli et al., 2008; Conti et al., 2014; Gaffen et al., 2011; Guglani and Khader, 2010; Korn et al., 2009; Ouyang et al., 2008; Romani, 2011; Yang et al., 2014). Murine Th17 cells induced by TGF-β1+IL-6 *in vitro* produce IL-17 but are incapable of inducing potent tissue inflammation upon adoptive transfer (Jäger et al., 2009; McGeachy et al., 2007) without additional stimuli, such as IL-1b and IL-23 (Awasthi et al., 2009; Chung et al., 2009; Cua et al., 2003; Ghoreschi et al., 2010; Lee et al., 2012; McGeachy et al., 2009). Therefore, there appear to be at least two different types of Th17 cells: homeostatic ones that do not promote tissue inflammation, to which we refer as non-pathogenic Th17 cells and ones that produce IL-17 together with interferon (IFN)g and granulocyte-macrophage colony-stimulating factor (GM-CSF) and induce tissue inflammation/autoimmunity, to which we refer as pathogenic Th17 cells (Lee et al., 2014). Distinct types of Th17 cells have also been identified in humans, where cells similar to mouse pathogenic Th17 cells are specific for immune response to *Candida albicans,* whereas cells similar to the non-pathogenic mouse Th17 are observed with *Staphylococcus aureus* infection (Zielinski et al., 2012). Thus, Treg, non-pathogenic Th17, and pathogenic Th17 cells represent a functional spectrum in tissue homeostasis, infection, and tissue inflammation *in vivo* and can be differentiated with different cytokine cocktails *in vitro*.

Metabolism is an established regulator of the Th17/Treg axis (Barbi et al., 2013). We hypothesized that metabolism similarly regulated the effector functions of Th17 subtypes. However, most cellular assays, including metabolic assays, are targeted and difficult to undertake at a single-cell resolution. Furthermore, low cell numbers may prohibit direct metabolic assays, for example, in the study of immune cells present at tissue sites. In contrast, scRNA-seq is broadly accessible and rapidly collected in concentrated efforts to reach a complete representation of human physiology (Regev et al., 2017). A computational method is thus required to capitalize on the opportunities afforded by scRNA-seq for contextualization of metabolic models, while systematically addressing the unique challenges of this data modality (e.g., its sparsity).

Here, we present Compass, an FBA algorithm that uses single-cell transcriptomic profiles to characterize cellular metabolic states at single-cell resolution and with network-wide comprehensiveness. Compass allows detection of targets across the entire metabolic network, agnostically of pre-defined metabolic pathway boundaries, and including ancillary pathways that are normally less studied yet important for cellular function (Puleston et al., 2017). We applied the algorithm to Th17 cells, uncovering substantial immunometabolic diversity associated with their inflammatory effector functions. In addition to differential wiring of central carbon metabolism, this analysis identified the polyamine pathway as a critical regulator of Th17 effector function, which we experimentally validated.

RESULTS

Compass—an algorithm for comprehensive characterization of single-cell metabolism

We reasoned that even though the mRNA expression of enzymes is not an accurate proxy for their metabolic activity, a global analysis of the metabolic network (as enabled by RNA-seq) in the context of a large sample set (as offered by single-cell genomics) coupled with strict criteria for hypotheses testing, would provide an effective framework for predicting cellular metabolic states. This led us to develop the Compass algorithm, which integrates scRNA-seq profiles with prior knowledge of the metabolic network to infer metabolic states of cells (Figure 1A).

The metabolic network is encoded in a genome-scale metabolic model (GSMM) that includes reaction stoichiometry, biochemical constraints such as reaction irreversibility, nutrient availability, and gene-enzyme-reaction associations. Here, we use Recon2, which is comprised of 7,440 reactions and 2,626 unique metabolites (Thiele et al., 2013). To explore the metabolic capabilities of each cell, Compass solves a series of constraint-based optimization problems (formalized as linear programs) that produce a set of numeric scores, one per reaction (STAR Methods). Intuitively, the score of each reaction in each cell reflects how well-adjusted is the cell's overall transcriptome to maintaining high flux through that reaction. Henceforth, we refer to the scores as quantifying the "potential activity" of a metabolic reaction (or "activity" in short when it is clear from the context that Compass predictions are discussed).

Compass belongs to the family of FBA algorithms that model metabolic fluxes (the rate by which chemical reactions convert substrates to products), through constrained-based optimization (Palsson, 2015). The first step of Compass is agnostic to gene expression and computes, for every metabolic reaction r, the maximal flux v_r^{opt} it can carry while imposing only

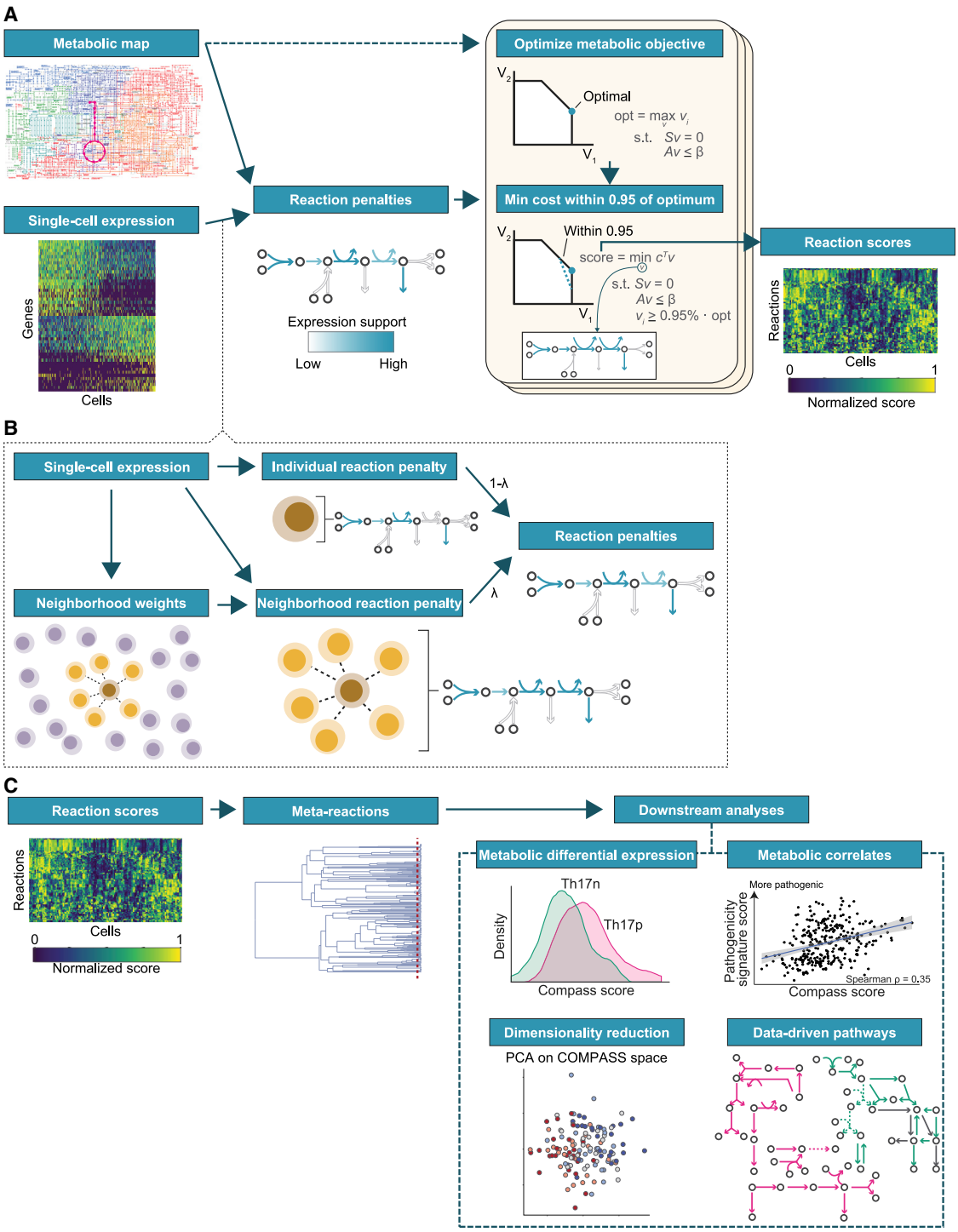

Figure 1. Algorithm overview

(A) Computation of Compass scores matrix. Compass leverages the topology and stoichiometry of the metabolic network to analyze single-cell RNA expression. Briefly, it computes a reaction-penalties matrix, where the penalty of a given reaction is inversely proportional to the expression of its respective enzyme-coding genes. The reaction-penalties matrix is the input to a set of flux-balance linear programs that produce a score for every reaction in every cell, namely the Compass score matrix.

(B) Soft information sharing between a cell and its k-nearest neighbors mitigates technical noise in single-cell data.

(C) Downstream analysis of the score matrix. Metabolic reactions are hierarchically clustered into meta-reactions; scores are used in differential expression of reactions, detection of reactions correlated with a phenotype of interest, dimensionality reduction, and data-driven network analysis.

See also Figure S1.

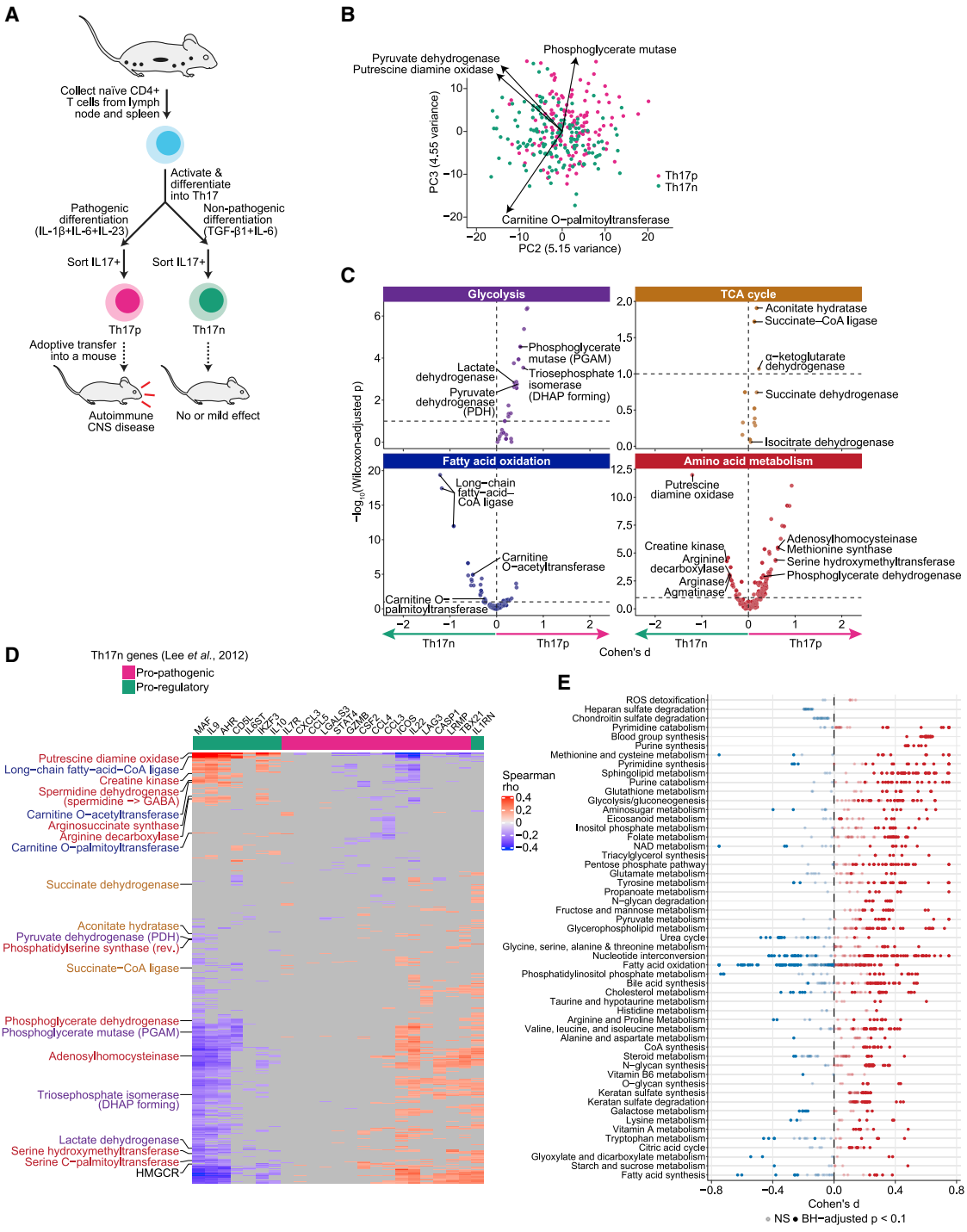

Figure 2. Compass-based exploration of metabolic heterogeneity in Th17 cells

(A) The experimental system. Naive CD4$^+$ T cells differentiated into pathogenic (Th17p) or non-pathogenic (Th17n) IL-17$^+$ T cells that cause severe or mild CNS autoimmunity upon adoptive transfer, respectively.

(B) PCA of the Compass score matrix with top loadings shown.

(C) Compass-score differential activity test between Th17p and Th17n cells (STAR Methods).

(legend continued on next page)

stoichiometry and mass balance constraints. Next, Compass assigns every reaction in every cell a penalty inversely proportional to the mRNA expression associated with the enzyme(s) catalyzing the reaction in that cell. Finally, for every reaction r and every cell, Compass finds a flux distribution (an assignment of flux values to every reaction in the network) that minimizes the overall penalty incurred, while maintaining a flux of at least $\omega \cdot v_r^{opt}$ (here, $\omega = 0.95$) through r. The additive inverse of this penalty term is the reaction score.

The use of genome-scale metabolic networks allows the entire metabolic transcriptome to impact the computed score for any particular reaction, rather than just the mRNA coding for the enzymes that catalyze it. We reasoned that this helps reduce the effect of instances where mRNA expression does not correlate with metabolic activity and of scRNA-seq dropouts (Wagner et al., 2016). Compass further mitigates data sparsity effects through information-sharing on a *k*-nearest neighbors graph, similar to other scRNA-seq algorithms (Baran et al., 2019; van Dijk et al., 2018; Grün, 2020; Haghverdi et al., 2018; Huang et al., 2018; Lun et al., 2016) (Figure 1B; STAR Methods).

The output of Compass is a quantitative profile for the metabolic state of every cell, which is then subject to downstream analyses (Figure 1C). The statistical power afforded by the large number of individual cells in a typical scRNA-seq study adds robustness and allows these downstream analyses to gain biological insight despite the high dimension of the metabolic space in which Compass embeds cells.

Th17 functional states are associated with metabolic states

We used Compass to study the metabolism of Th17 cells differentiated *in vitro* into two extreme functional states (Figure 2A)—pathogenic (Th17p) and non-pathogenic (Th17n). We analyzed a dataset we generated in a previous study that included 139 Th17p and 151 Th17n cells sorted for IL-17A/GFP$^+$ (Gaublomme et al., 2015; Wang et al., 2015). We computed Compass scores and aggregated reactions that were highly correlated across the entire dataset (Spearman's rho $\geq$0.98) into meta-reactions (median of two reactions per meta-reaction) (Figure S1A) for downstream analysis. We tested the robustness of Compass by running the algorithm on the same gene expression input with added random noise. The deviation of the noised Compass scores from the original output did not exceed the deviation induced by the noise to the gene expression input (Figures S1B–S1C).

To investigate the main determinants of metabolic heterogeneity between Th17 cells, we first analyzed the Compass output as a high dimensional representation of the cells that parallels the one produced by scRNA-seq but with features corresponding to metabolic meta-reaction rather than genes. We performed principal component analysis (PCA) on the meta-reaction matrix, while restricting it to 784 meta-reactions (out of 1,911) that are associated with core metabolism (STAR Methods), spanning conserved and well-studied pathways for generation of ATP and synthesis of key biomolecules.

The first two principal components (PCs) were associated with overall metabolic activity and T effector functions (Figures 2B, S2A, and S2B; Table S1). PC1 correlated with the cell's total metabolic activity, defined as the expression ratio of genes coding metabolic enzymes out of the total protein coding genes (Pearson's rho = 0.36, $p < 4e{-}10$), as well as a transcriptional signature of late stages of Th17 differentiation over time (Yosef et al., 2013) (Figure S2C) (Pearson's rho = 0.18, $p < 0.003$) (STAR Methods). PC2 and PC3 represented a choice between ATP generation through aerobic glycolysis versus fatty acid oxidation, similar to previous observations in comparisons of Th17 to Tregs, or Teff to Tmem (Geltink et al., 2018). Accordingly, these PCs correlated with multiple Th17 pathogenicity markers, as well as a signature of Th17 pathogenicity consisting of cytokines, chemokines, and transcription factors (TFs) that are associated with each phenotypic group (Lee et al., 2012) (Figures S2D and S2E). PC2 and PC3 were also associated with nitrogen metabolism and were enriched in urea cycle targets whose power to modulate Th17 pathogenicity is demonstrated below.

Compass predicts metabolic regulators of Th17 cell pathogenicity

To detect metabolic targets associated with the pathogenic capacity of individual Th17 cells, we defined pro-pathogenic and pro-regulatory reactions as ones that were significantly differentially active in Th17p or Th17n, respectively (Figures 2C and S2F; Table S2; STAR Methods) (1,213/6,563 reactions, Benjamini-Hochberg [BH] adjusted Wilcoxon rank-sum $p < 0.001$). Many of these reactions were also correlated with the expression of cytokines and TFs relevant for Th17 function (Figures 2D and S2G; Table S3) (note that these genes do not code metabolic enzymes and thus were not used by Compass). Notably, many classically defined metabolic pathways included both reactions predicted to be pro-pathogenic and pro-regulatory (Figure 2E), highlighting the value in examining single reactions within a global network rather than conducting a pathway-level analysis. A similar result is obtained at the gene expression level—many metabolic pathways included both genes that were upregulated and genes that were downregulated in Th17p compared to Th17n (Figure S2H).

Compass highlighted differences in central carbon metabolism between the Th17p and Th17n states, which mirror those found between Th17 and Treg. The algorithm predicted that glycolytic reactions were generally more active in Th17p than in Th17n (Figures 2C and 3A). This parallels previous results showing that Th17 upregulate glycolysis, and failure to do so promotes a Treg fate (Gerriets et al., 2015; Michalek

(D) Spearman correlation of Compass scores with the expression of pro-pathogenic (magenta) or pro-regulatory (green) Th17n genes (Lee et al., 2012). Non-significant correlations (BH-adjusted $p \geq 0.1$) shown in gray. Rows are 489 meta-reactions that belong to core pathways (STAR Methods), and significantly correlated or anti-correlated with at least one of the genes.

(E) Differential activity (as in C) of metabolic reactions. Reactions (dots) are partitioned by Recon2 pathways and colored by the sign of their Cohen's d statistic. See also Figure S2 and Tables S1, S2, and S3.

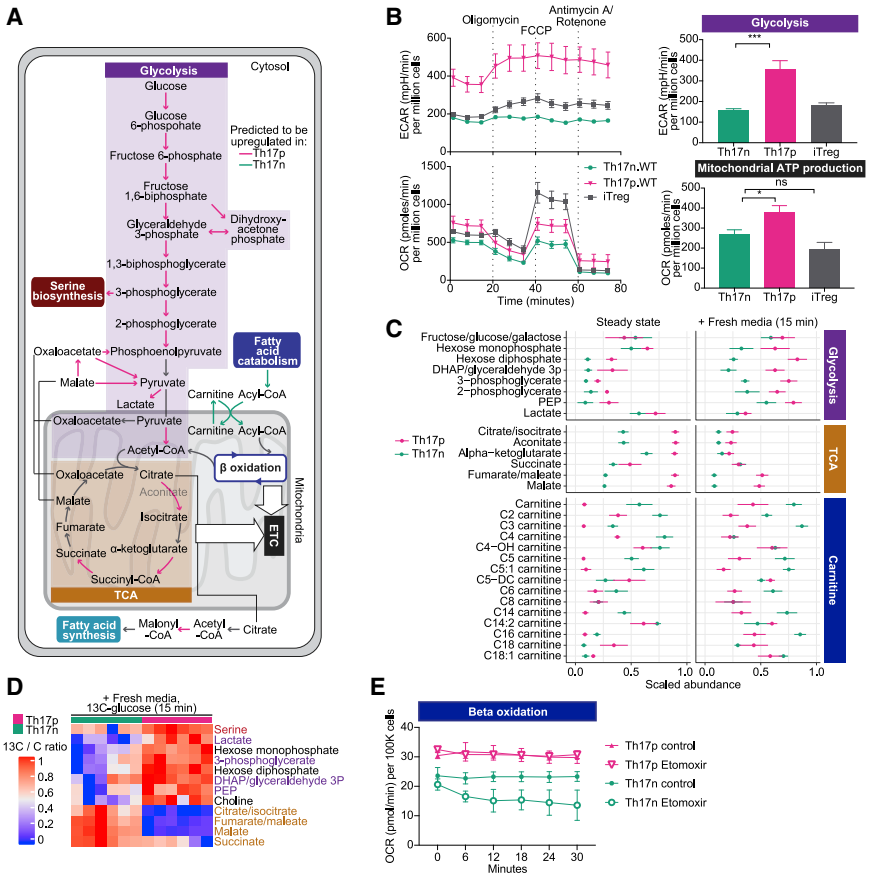

Figure 3. Differential usage of glycolysis and fatty acid oxidation by pathogenic and non-pathogenic Th17 cells

(A) Central carbon metabolism overlaid with Compass predictions for differentially active reactions; Th17p versus Th17n, BH-adjusted Wilcoxon rank-sum $p < 0.1$ denoted in non-gray.

(B) Mito stress test by Seahorse assay of differentiated T cells (68 h).

(C and D) LC/MS metabolomics (n = 6 mice; C shows means and SE error bars) of cells harvested at 68 h (C, left), replated in fresh media with no additives (C, right), or with ^{13}C-tagged glucose for 15 min (D). (D) The ratio of ^{13}C-tagged carbon out of the total carbon content associated with the metabolite.

(E) T cells were measured for their oxygen consumption rate measured in T cells with control or 40 μM etomoxir (n = 2, each with 6 mouse replicates).

See also Figure S3.

et al., 2011; Shi et al., 2011). Compass also predicted an increased activity in Th17p through two segments of the TCA cycle, but not the cycle as a whole (Figures 2C and 3A). A similar breakdown of the TCA cycle in relation with pro-inflammatory function has been described in macrophages where M1 polarization divided the TCA cycle at the same two points: isocitrate dehydrogenase (Jha et al., 2015) and succinate dehydrogenase (Mills et al., 2016), which supported macrophage inflammatory functions (Mills and O'Neill, 2014; Shi et al., 2019).

In fatty acid (FA) metabolism, Compass predicted that cytosolic acetyl-CoA carboxylase (ACC1), the committed step toward FA synthesis, was upregulated in Th17p, whereas the first two steps of long-chain FA oxidation (long chain fatty acyl-CoA synthetase and carnitine O-palmitoyltransferase [CPT]) were predicted to be higher in Th17n. These predictions mirror a known metabolic difference between the Th17 and Treg lineages, where Th17 rely on *de novo* FA synthesis (Berod et al., 2014), whereas Tregs scavenge them from their environment and catabolize them and produce ATP through beta-oxidation (Michalek et al., 2011; Pompura et al., 2021). We note, however, that recent evidence suggests that CPT may be upregulated in Treg over Th17 but is not functionally indispensable for Treg to obtain their effector phenotypes (Raud et al., 2018).

Multiple amino-acid metabolism reactions were also differentially active between Th17p and Th17n (Figure 2C; Table S2). Amino acids are important for Th17 cell differentiation (Sundrud et al., 2009), and Compass adds further granularity to these findings. In particular, it predicted that serine biosynthesis from 3-phosphoglycerate and three downstream serine fates—sphingosines, choline, and S-adenosyl-methionine (SAM)—were higher in Th17p. On the other hand, parts of urea cycle and arginine metabolism are significantly associated with both Th17 states, (Figure 2C), suggesting that alternative fluxing within this subsystem may be associated with diverging Th17 cell function.

Pathogenic Th17 maintain higher aerobic glycolysis and TCA activity, whereas non-pathogenic Th17 oxidize fatty acids to produce ATP

We validated the Compass prediction that Th17p and Th17n differ in their central carbon metabolism (Figure 3A). First, we assayed glycolysis and mitochondrial function of Th17 cells (Figure 3B). Th17p had higher extracellular acidification rate (ECAR) than Th17n, indicating accumulation of lactate due to aerobic glycolysis. Th17p also generated more ATP in a mitochondria-dependent fashion, consistent with the predicted higher entrance of pyruvate into the TCA cycle despite the diversion of some pyruvate toward the lactate fate.

Liquid chromatography-mass spectrometry (LC/MS) metabolomics indicated that glycolytic metabolites were higher in Th17p than in Th17n (Figure 3C, top). When further pulsed with fresh media containing glucose for 15 min, there was a substantial increase in glycolytic metabolites in Th17p but less so in Th17n. After 3 h, the level of these metabolites decreased back to steady state (Figure S3A). TCA metabolites, apart from succinate, were more abundant at steady state in Th17p than in Th17n (Figure 3C, middle), consistent with Compass prediction that two parts of the TCA cycle, but not the cycle as a whole, were upregulated

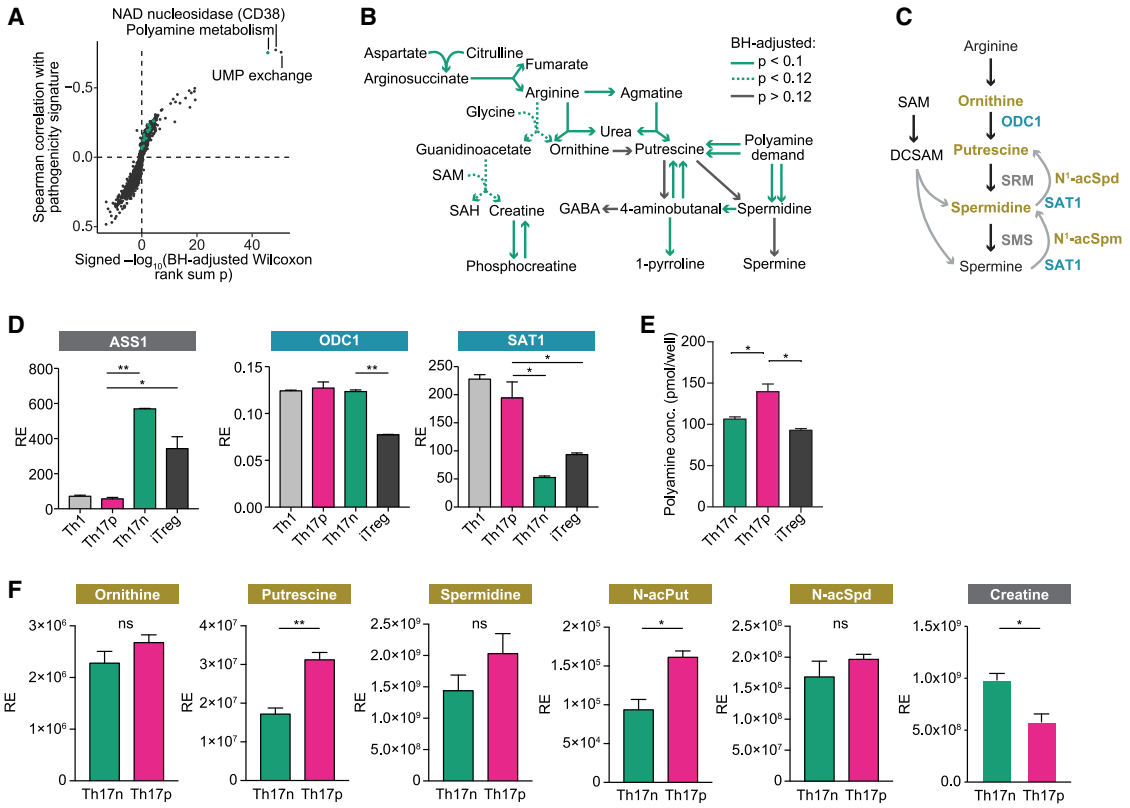

Figure 4. Prediction and metabolic validation of the polyamine pathway as a regulator of Th17 function

(A) x axis: Compass-score differential activity test; Th17p versus Th17n. BH-adjusted Wilcoxon rank-sum p signed by the direction of change. y axis: Spearman correlation between Compass scores and cell pathogenicity scores (STAR Methods). Dots are meta-reactions, and green dots are meta-reactions containing at least one reaction that appears in the network of (B). All reactions comprising the meta-reaction labeled "polyamine metabolism" are denoted in (B).

(B) A metabolic network that is preferentially active in Th17n based on Compass results. Green arrows represent reactions predicted to be significantly associated with the Th17n program; double arrows are reactions belonging to the meta-reaction labeled "polyamine metabolism" in (A). SAM, S-adenosyl-methionine; SAH, S-adenosyl-homocysteine; GABA, gamma-aminobutyric acid.

(C) Schematic polyamine pathway based on KEGG.

(D–F) T cells were differentiated (STAR Methods) (shown is a representative of 2–3 experiments with 3–4 mice each) and harvested at 48 h for qPCR (D) and 68 h for polyamine enzymatic assay (E) and metabolomics (E and F).

See also Figure S4 and Table S2.

in Th17p. Therefore, both Compass and the metabolomics data point to succinate as a potential metabolic control point.

To test whether not only absolute metabolite levels, but also the relative allocation of carbon into alternative fates, differ between Th17p and Th17n, we performed carbon tracing with ^{13}C-glucose. Consistent with our predictions, Th17p had higher relative abundance of ^{13}C-labeled glycolytic metabolites (Figure 3D). Furthermore, Th17p preferentially incorporated glucose-derived carbon into serine (that branches from glycolysis) (Figure S3B) and its downstream product choline (Figure 3D), confirming a Compass prediction (Figure 2C). Conversely, Th17p had lower relative abundance of ^{13}C-labeled TCA metabolites (Figure 3D), suggesting that the higher level of TCA intermediates observed in Th17p at steady state (Figure 3C) might not be supported from glucose, but rather from other sources (Johnson et al., 2018; Pucino et al., 2019). Taken together, our results suggest that Th17p cells have higher overall activity through the TCA cycle at steady state but quickly switch to aerobic glycolysis when glucose is readily available in the environment.

We next validated the prediction that Th17n cells prefer beta-oxidation. Metabolomics analysis shows that Th17n were enriched in acyl-carnitine metabolites, particularly short- to medium-length acyl groups (Figures 3C and S3A), indicating active lipid transport through the mitochondrial membrane. When etomoxir was used to block acyl-carnitine transportation, oxygen consumption rate decreased in Th17n but not Th17p (Figure 3E). Although etomoxir has off-target effects (Divakaruni et al., 2018; Raud et al., 2018), overall our data support the hypothesis that Th17n cells ultimately divert fatty acid breakdown products into the electron transport chain to generate ATP.

Identifying the polyamine pathway as a candidate regulator of Th17 function

The polyamine pathway stood out as one of the most significantly associated with differences in Th17 pathogenicity

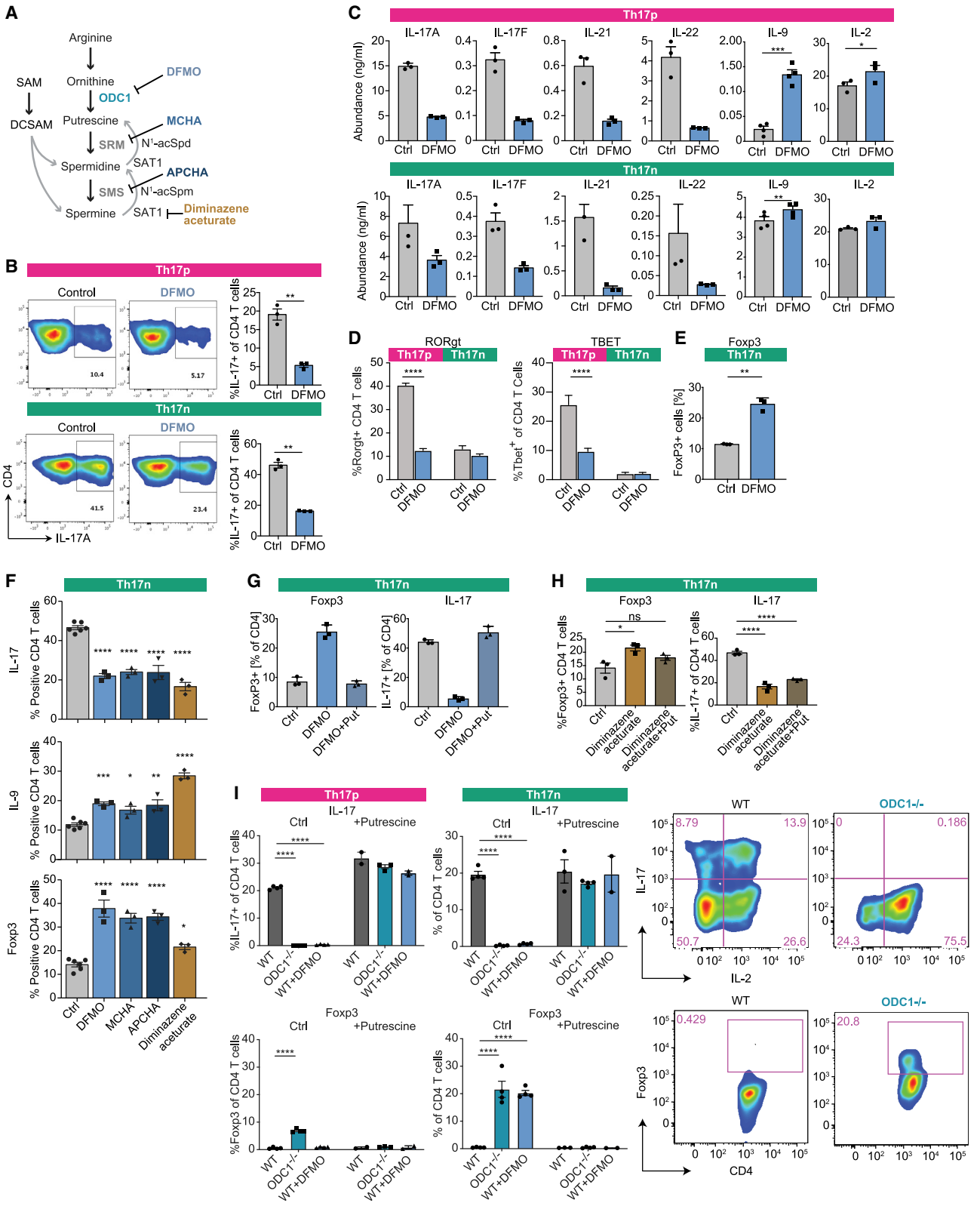

(legend on next page)

according to Compass predictions (Figure 4A; Table S2). We constructed a data-driven metabolic network anchored around putrescine, the starting metabolite in canonical polyamine synthesis, by including adjacent metabolites whose reactions are predicted to be associated with pathogenicity (Figure 4B). Although several polyamine-associated genes were differentially expressed between Th17p and Th17n, the network tied the differential polyamine metabolism to differences in upstream and downstream metabolic reactions that could not be captured from differential gene expression directly. Specifically, Compass predicted that Th17n cells are more active in arginine metabolic pathways, upstream of putrescine, and in alternative fates of putrescine (other than conversion to spermidine along the canonical polyamine synthesis pathway).

Cellular polyamines are suppressed in regulatory T cells and non-pathogenic Th17

We asked whether critical enzymes of the polyamine pathway (Figure 4C) were differentially expressed between $CD4^+$ T cell subsets using qPCR. Ornithine decarboxylase 1 (ODC1) and spermidine/spermine N1 acetyltransferase 1 (SAT1) are the rate-limiting enzymes of polyamine biosynthesis and catabolic processes, respectively. SAT1 level was higher in Th17p than in Th17n or Treg, whereas ODC1 was similarly expressed in Th17n and Th17p but significantly lower in Treg. Interestingly, argininosuccinate synthetase 1 (ASS1), an enzyme upstream of polyamine biosynthesis was upregulated in Th17n, consistent with Compass-predicted alternative flux in the polyamine neighborhood (Figure 4D). Collectively, these data suggest that the polyamine pathway may be associated with functional state in Th17 and other T cell lineages.

We next measured polyamine metabolites using an enzymatic assay and LC/MS metabolomics (STAR Methods). Compared to Th17p, Treg and Th17n had reduced levels of total polyamines (Figure 4E), reflecting reduced import, reduced biosynthesis, or increased export of polyamines in these cells. We then measured metabolites in the polyamine neighborhood (Figures 4F and S4A). Consistent with Compass's predictions, there was higher creatine content in Th17n than in Th17p. Although cellular ornithine (polyamine precursor) was comparable between Th17p and Th17n, Th17p had higher levels of putrescine and acetyl-putrescine (Figure 4F). Of note, cellular spermidine and acetyl-spermidine were not different between the conditions, and spermine was not detected (Figure 4F). The reduced putrescine and its acetyl form in Th17n are unlikely due to increased export, because we observed very little polyamines in the media of either Th17n or Th17p (Figure S4A). These data suggest that polyamines accumulate within Th17p and that the main function of SAT1 in Th17p may be to recycle rather than to export polyamines.

Arginine and citrulline can be used to synthesize the polyamine precursor ornithine. We used carbon- or hydrogen-labeled arginine or citrulline to study polyamine biosynthesis (Figures S4B and S4C). We harvested cells and media for LC/MS at 0, 1, 5, and 24 h post addition of labeled arginine. Although labeled cellular guanidinoacetic acid, a byproduct of arginine conversion into ornithine, was comparable between Th17n and Th17p, over time Th17p cells accumulated more intracellular putrescine, acetyl-putrescine, and acetyl-spermidine (Figure S4B), consistent with increased polyamine biosynthesis and/or recycling activity in these cells. Conversely, Th17n accumulated more labeled arginine than Th17p. This prompted us to investigate whether Th17n can also better synthesize (as opposed to better uptake) arginine, which would be consistent with higher ASS1 expression (Figure 4D) in these cells. We pulsed cells with labeled citrulline, an arginine precursor, and indeed observed higher levels of labeled arginine in Th17n (Figure S4C). Collectively, the targeted metabolomics and tracing data suggest that Th17n accumulate arginine, and Th17p preferentially synthesize or recycle polyamines. We conclude that differences in polyamine biosynthesis are associated with the different Th17 functional states.

ODC1 or SAT1 inhibition restricts Th17 function in a putrescine-dependent manner

We studied the effects of polyamine pathway inhibitors on Th17 differentiation *in vitro*. Difluoromethylornithine (DFMO), an irreversible inhibitor of ODC1, suppressed polyamines and inhibited IL-17 expression in both Th17n and Th17p (Figures 5A, 5B, and S5A). DFMO also inhibited the expression of other canonical Th17 cytokines such as IL-17A, IL-17F, IL-21, and IL-22, while promoting IL-9 levels in culture supernatant (Figure 5C). IL-17 inhibition does not appear to be solely related to IL-2 regulation (Bowlin et al., 1987), because DFMO promoted IL-2 expression in Th17p, but not Th17n (Figure 5C). In support of this view, IL-2 neutralization did not rescue the inhibitory effects of DFMO (Figures S5B–S5E). DFMO reduced cell proliferation (data not shown) and this likely contributed to its suppression of Th17 effector functions. However, when considering only cells that had divided exactly once as means to select cells that are equally potent proliferators, DFMO treatment led to a lower frequency of $IL\text{-}17^+$ cells (data not shown). Therefore, DFMO can regulate Th17 also independently of proliferation. The increased secretion of IL-9 (a Th9 cytokine) by DFMO-treated cells also suggests that DFMO does not inhibit Th17 function solely by reducing cell viability.

Figure 5. Chemical and genetic perturbations of the polyamine pathway suppress canonical Th17 cytokines

(A) Polyamine pathway schematic depicting chemical inhibitors.

(B–E) Flow cytometry of differentiated cells on day 3 (d3); (B), (D), and (E) intracellular staining; (C) secreted cytokines by LEGENDplex. DFMO or solvent control (water) was added at d0.

(F) Inhibition of polyamine pathway targets in *in vitro* differentiated Th17n.

(G and H) Addition of 2.5 mM putrescine has a rescue effect in cultures with inhibited ODC1 (G) or SAT1 (H).

(I) Flow cytometry of T cells differentiated from WT or $ODC1^{-/-}$ mice under the indicated conditions (n = 4 mice). Statistical significance computed by paired t test or one-way ANOVA, as appropriate for the context, with Bonferroni adjustment for multiple comparisons.

See also Figure S5.

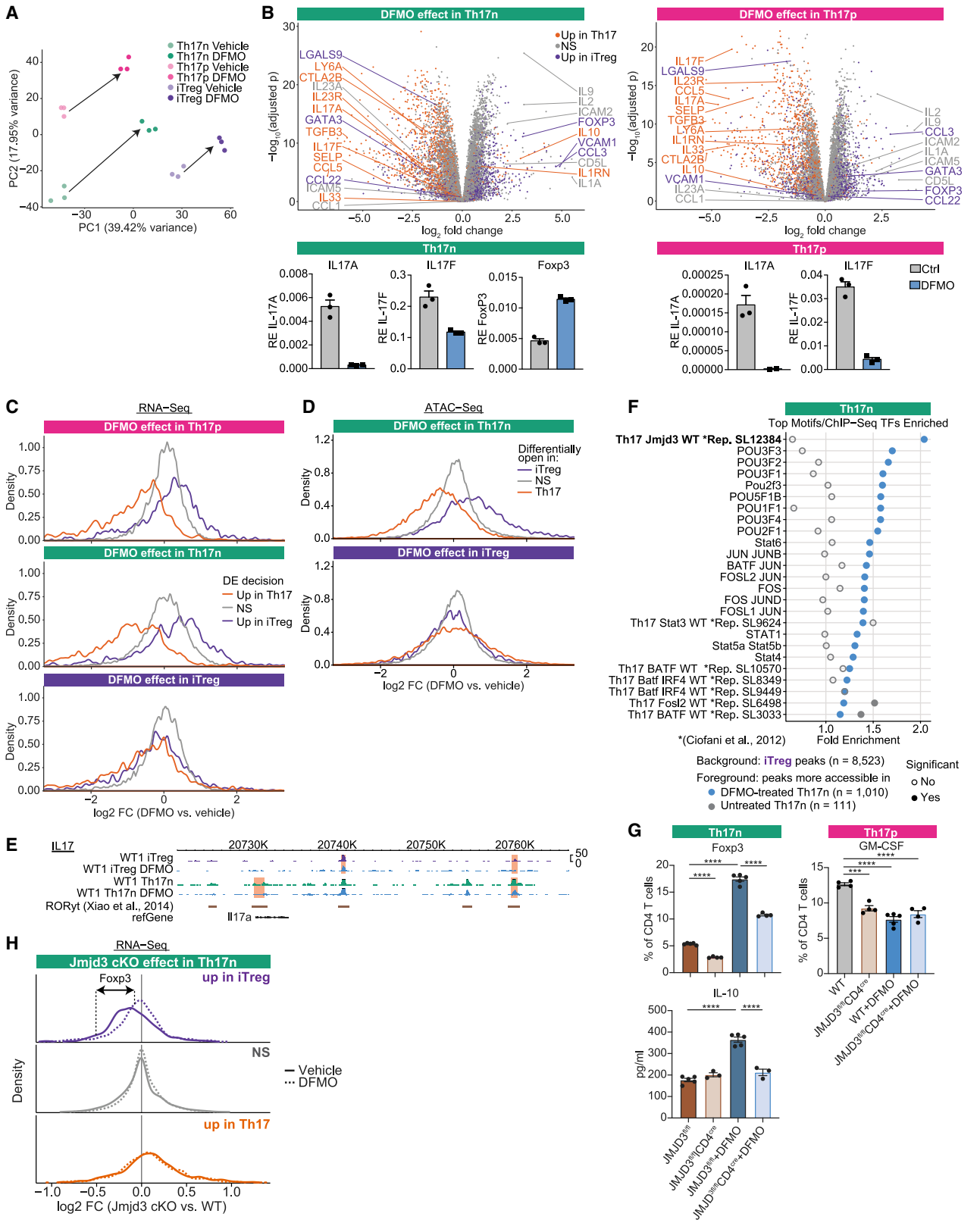

(legend on next page)

Turning to Th17 transcription factors, DFMO suppressed Rorgt and Tbet expression in Th17p but not Th17n (Figure 5D), suggesting a nuanced effect. Consistently, DFMO decreased pStat3, and not total Stat3 protein levels, only in Th17p (Figure S5F). IL-17 inhibition is not due to increased Foxo1 activity, another critical regulator of Th17 function, because DFMO promoted pFoxo1(S256) (Figure S5F). Given the reciprocal regulation of Th17 and Treg, and because DMFO also impacted polyamine levels in Tregs (Figure S5A), we asked whether DFMO regulates Foxp3 even under Th17 differentiation conditions. DFMO increased the frequency of Foxp3^{+} cells in Th17n but not Th17p (Figure 5E), presumably because TGF-β1 is required for Foxp3 expression.

To determine whether other enzymes of the polyamine pathway also regulate Th17 function, we used inhibitors of spermine synthase (SRM) and spermidine synthase (SMS) (Figure 5A). Similar to DFMO, inhibitors of any of the biosynthesis enzymes suppressed IL-17 and promoted IL-9 and Foxp3 expression, the latter in Th17n (Figure 5F). Furthermore, using diminazene aceturate to inhibit SAT1, a rate-limiting enzyme of polyamine acetylation and recycling, had similar effects (Figure 5F). SAT1 and ODC1 are probably part of a self-regulating feedback loop, because perturbation in one was previously reported to affect the other (Jell et al., 2007; Mounce et al., 2016; Pegg, 2008). Consistent with this finding, inhibition of ODC1 with DFMO suppressed SAT1 expression in Th17 cells (Figure S5G).

Finally, we confirmed that the effect of DFMO was through inhibition of ODC1, as addition of putrescine to cells treated with DFMO completely reversed their phenotype (Figure 5G). Interestingly, addition of putrescine with SAT1 inhibition partially reversed the upregulation of Foxp3, but not the suppression of IL-17 (Figure 5H). This suggests that ODC1 and SAT1 have not only shared but also (despite their proximity in the metabolic network) distinct functions in the regulation of the T effector program.

ODC1$^{-/-}$ Th17 cells upregulate Foxp3 expression

To further confirm the effects of polyamine pathway inhibition on T cells, we differentiated Th17 cells from wild-type (WT) and ODC1$^{-/-}$ mice. Similar to DFMO treatment, there was complete inhibition of Th17 canonical cytokines, such as IL-17A, IL-17F, and IL-22, but not IFNg, in ODC1$^{-/-}$ Th17 cells (Figures 5I and S5H). Although ODC1 deficiency did not lead to a decrease in Rorgt expression (data not shown), the loss of Th17 canonical cytokines is consistent with loss of the Th17 program. Furthermore, ODC1$^{-/-}$ Th17n upregulated Foxp3, consistent with promotion of a Treg program (Figure 5I). Finally, the observed effects of ODC1$^{-/-}$ were rescued by addition of putrescine (Figures 5I and S5H).

DFMO restricts Th17-cell transcriptome and epigenome in favor of Treg-like state

To gain mechanistic insight, we profiled bulk RNA from Th17p, Th17n, and iTreg cells treated with DFMO or control (STAR Methods). DFMO had a profound impact on the transcriptome of all three lineages, driving Th17 cells toward a Treg profile (Figure 6A). We next determined the aggregate effect of DFMO on genes that are upregulated (n = 1,284), downregulated (n = 1,255), or comparable (n = 8,257) in untreated Th17 versus Treg (Figure 6B). In both Th17p and Th17n, DFMO suppressed the Th17-specific in favor of the Treg-specific transcriptome (Figure 6C; Tables S4 and S5). Canonical Th17 cell genes such as IL17a, IL17f, and IL23r were suppressed, whereas Treg-related genes, such as Foxp3 and CCL3, were upregulated (Figure 6B). There was no consistent effect of DFMO on Treg or genes expressed comparably in Th17 and Treg (Figure 6C). Thus, the polyamine pathway is important for restricting the Treg-like program in Th17 cells in both Th17p and Th17n states.

DFMO also promoted a subset of genes that are characteristic to Th17n but not to Th17p or iTreg (Figure S6A; Table S6). Notably, DFMO treatment in both Th17n and Th17p led to elevated levels of the pro-regulatory IL-9 transcript (Lee et al., 2012), consistent with the aforementioned protein analysis (Figure 5C) and the initial Compass prediction (Figure 2D). This accords with polyamine metabolism promoting Th17 over Treg fate on the one hand, while being associated with a Th17n fate (marked by high IL-9 expression) over Th17p on the other. Furthermore, DFMO-treated Th17 upregulated the CD5L/AIM transcript, which we showed to be predominantly expressed by Th17n (Wang et al., 2015).

Although DFMO profoundly altered the Th17 transcriptome, it did not consistently restrict phosphorylation of key Th17 cell regulators, particularly not in Th17n (Figure S5F). We hypothesized that polyamines may impact the epigenome, which was also suggested by the altered expression of many chromatin modifiers in DFMO-treated cells (Figure S6B). To test this hypothesis, we measured chromatin accessibility by ATAC-seq

Figure 6. DFMO treatment promotes Treg-like transcriptome and epigenome

T cells were harvested at 68 h for live cell-sorting and population RNA-seq (A–C) and ATAC-seq (D–F).

(A) PCA plot of the RNA-seq.

(B) Volcano plots (upper) and qPCR validation (lower) of genes affected by DFMO treatment.

(C and D) Density plot showing DFMO effects on transcriptome (C) and chromatin accessibility (D). Genes or loci are divided into those upregulated or more accessible, respectively, in Th17 cells (orange), Treg (violet) or neither (gray) (STAR Methods).

(E) IGV plots of IL17a region; Rorgt binding sites with significantly altered accessibility by DFMO are highlighted. A representative (WT1) of 3 mice is shown.

(F) Rows show hypergeometric enrichment computed for peaks annotated with a genomic feature by ChIP-seq (Ciofani et al., 2012) or DNA binding motifs (STAR Methods). Dots are fold enrichment of peaks more accessible in DFMO-treated (blue) or untreated (gray) Th17n against a background of iTreg peaks.

(G) Differentiated cells were rested at 68 h and harvested at 120 h for analysis of intracellular Foxp3 or GM-CSF, and IL-10 secretion. BH-adjusted ****$p < 0.0001$; ***$p < 0.001$. A representative of 2 experiments with 4 mice each.

(H) Cells from (G) were harvested at 68 h for RNA-seq (n = 4). Density plots showing JMJD3 deficiency and DFMO treatment effects. Treg and Th17 programs were defined similarly to (C).

See also Figure S6 and Tables S4, S5, S6, and S7.

in Th17n and iTreg cells (STAR Methods). Overall, DFMO treatment resulted in considerable changes in accessible regions in both lineages (Figure S6C). We asked whether DFMO preferentially altered accessibility in Th17- and Treg-specific regions by partitioning all accessible peaks into those more accessible (n = 10,431), less accessible (n = 3,421), or comparably accessible (n = 34,591) in untreated Th17n versus Treg (Figure 6D). Consistent with the RNA-seq data, DFMO restricted accessibility in Th17-specific regions and favored accessibility in Treg-specific regions (Figure 6D; Tables S5 and S7). Differentially accessible regions were found near loci encoding key effector molecules (Table S7). For instance, DFMO restricted peaks in the promoter and intergenic regions of IL17a-IL17f that correspond to Rorgt binding sites known to regulate IL-17 expression (Figure 6E) (based on a chromatin immunoprecipitation sequencing [ChIP-seq] of Th17 cells by Xiao et al. [2014]). Thus, DFMO can shape chromatin accessibility in favor of a Treg epigenomic landscape, and this may contribute to the emergence of a Treg-like transcriptional program in DFMO-treated Th17 cells.

The chromatin regulator JMJD3 maintains Treg-like state in Th17 cells in a polyamine-dependent manner

To investigate which TFs may be responsible for the suppression of the Th17-specific program and upregulation of the Treg program, we looked for putative binding sites overlapping with regions whose accessibility is modulated by DFMO. When considering genomic regions that are typically more accessible in Tregs compared to Th17 and may be modulated by DFMO (Figures 6F and S6D; Table S7), we found that in Th17n cells, DFMO increased chromatin accessibility near potential binding sites of JMJD3 along with a number of POU-domain containing TFs.

Because JMJD3 regulates T cell plasticity (Ciofani et al., 2012; Li et al., 2014; Liu et al., 2015), we tested whether the transcriptional shifts induced by DFMO were altered in $JMJD3^{fl/fl}CD4^{cre}$ T cells. JMJD3 deficiency reduced Foxp3 expression and abrogated the upregulation of Foxp3 and IL-10 by DFMO in Th17n (Figure 6G). On the other hand, both JMJD3 deficiency and ODC1 inhibition suppressed GM-CSF expression in Th17p (Figure 6G). Of note, DFMO did not alter JMJD3 expression in Th17 cells (data not shown). These data suggest that JMJD3 and ODC1 have both distinct and overlapping functions. Consistent with the flow cytometry data, JMJD3 deficiency in Th17n resulted in a global transcriptome-wide shift restricting the Treg and (to a lesser extent) promoting the Th17 program (Figure 6H; Table S5). This agrees with previous findings that JMJD3 ablation *in vivo* promoted intestinal Th17 differentiation (Li et al., 2014). Notably, ODC1 inhibition by DFMO abolished the suppression of the Treg program by JMJD3 deficiency (differences between solid and dotted curves in Figures 6H and S6E; Table S5). However, the milder transcriptomic shift toward the Th17 program in $JMJD3^{fl/fl}CD4^{cre}$ mice was not reversed with further ODC1 inhibition by DFMO. In the other direction, JMJD3 had little global impact on the effects of DFMO (Figure S6F). We conclude that JMJD3 requires uninhibited ODC1 activity to sustain the Treg program, whereas the promotion of the Th17 program and the suppression of the Treg program by ODC1 activity do not require JMJD3.

Perturbation of ODC1 and SAT1, key enzymes of the polyamine pathway, alleviates EAE

We investigated the polyamine pathway *in vivo* in the context of EAE, a CNS autoimmune disease, via two approaches: chemical inhibition of ODC1 and T cell-specific genetic deletion of SAT1 (Figure 7). Because targeting multiple nodes in the polyamine pathway upregulated Foxp3 during Th17 differentiation *in vitro* (Figures 5 and 6), we hypothesized that perturbing rate-limiting enzymes *in vivo* would regulate the induction of EAE.

We first tested ODC1 inhibition by adding DFMO to the drinking water of mice immunized with MOG/CFA for EAE induction. DFMO delayed the onset and severity of EAE (Figure 7B), and reduced antigen-specific recall responses as measured by T cell proliferation in the draining lymph node (dLN) (Figure 7C). Further analysis of T cells isolated from the CNS showed no difference in cytokine production but increased frequency of $Foxp3^{+}$ $CD4^{+}$ T cells (Figure 7D and data not shown). These results agree with polyamine biosynthesis regulating the Th17/Treg balance in favor of Th17 and consequently, the induction of autoimmune CNS inflammation.

Because administration of DFMO via drinking water could affect multiple cell types, we also genetically deleted SAT1 in $CD4^{+}$ T cells ($SAT1^{fl/fl}CD4^{cre}$). We confirmed that genetic SAT1 deficiency in Th17 abrogated polyamine acetylation (Figure 7E). Notably, loss of SAT1 also reduced (non-acetylated) putrescine levels, supporting a feedback mechanism as discussed above (Figure S5G).

We observed delayed onset and severity of EAE in $SAT1^{fl/fl}CD4^{cre}$ mice (Figure 7F), as well as inhibition of antigen-specific recall responses (Figure 7G), similar to the effects observed with DFMO treatment. Although cytokine production was unaltered *ex vivo* by SAT1 deficiency, there was a trend toward decreased antigen-dependent IFNg, IL-17, and TNF production, and increased IL-9 (Figure 7H and S7A). $Foxp3^{+}CD4^{+}$ T cells were increased with a concomitant decrease of $Rorgt^{+}CD4^{+}$ T cells isolated from the CNS of $SAT1^{fl/fl}CD4^{cre}$ mice (Figure 7I). Notably, the frequencies of $Foxp3^{+}$ or $Rorgt^{+}$ cells were not different in dLN (Figure S7B), suggesting that the effect of SAT1 on T cells may be amplified in tissue recall responses. In conclusion, we demonstrated using both chemical and genetic perturbations at multiple levels that the polyamine pathway is an important mediator of autoimmune inflammation.

DISCUSSION

We presented Compass, an FBA algorithm, to study metabolism in single-cell transcriptomic data and validated a number of its predictions by molecular and functional analyses. These results support the power of transcriptomic-based FBA to make valid predictions in a mammalian system. The network-wide approach enabled Compass to successfully predict metabolic targets in both central and ancillary pathways.

Static FBA assumes that the system under consideration operates in chemical steady state (Varma and Palsson, 1994).

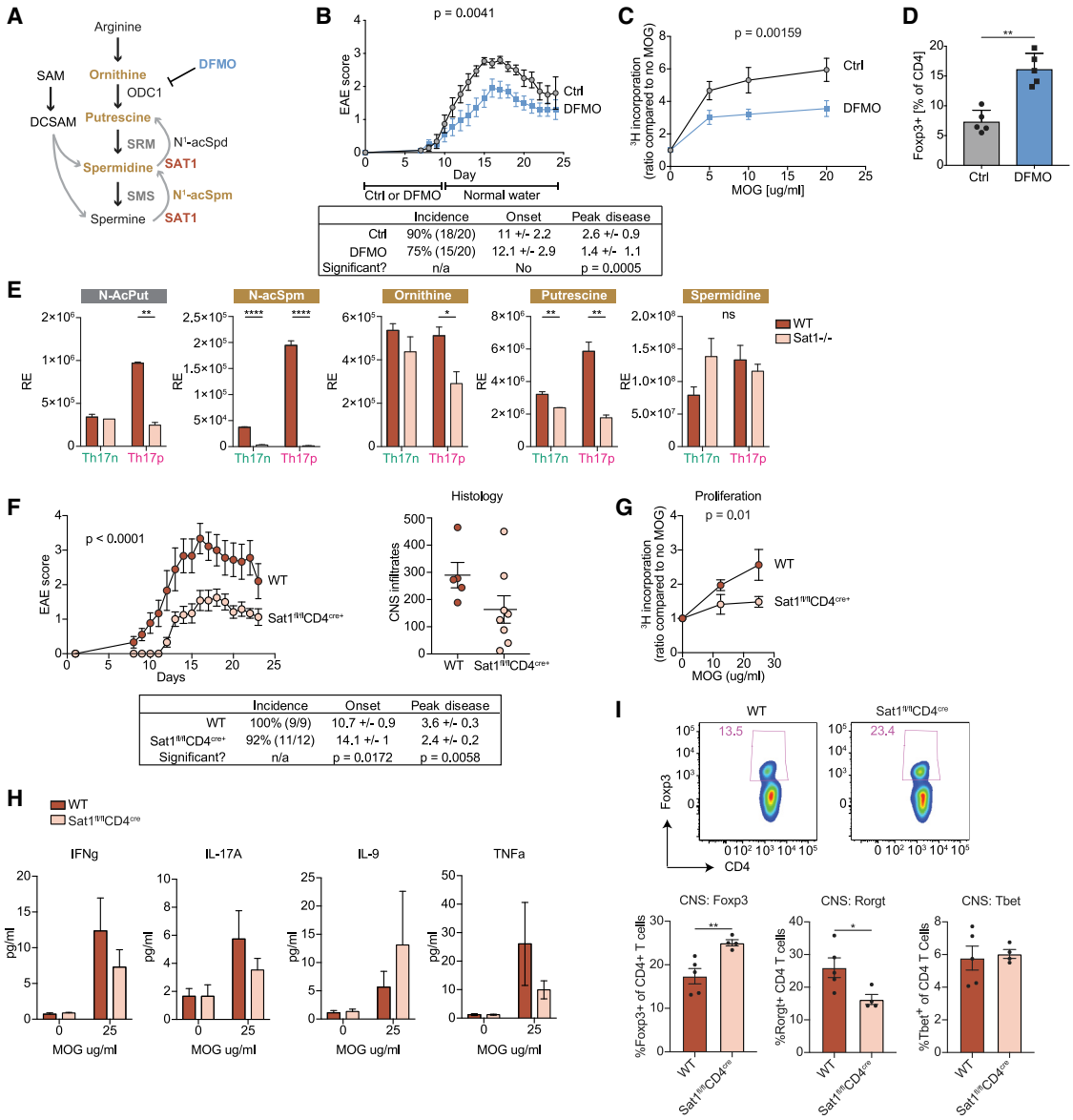

Figure 7. Targeting ODC1 and SAT1 alleviates experimental autoimmune encephalomyelitis (EAE)

(A) Polyamine pathway schematics.

(B–D) Effects of chemical inhibition of ODC1 by DFMO in drinking water on $MOG_{35–55}$/CFA induced EAE in wild-type mice.

(B) Clinical score over time.

(C) Antigen-specific proliferation of cells isolated from draining lymph node (dLN) at d23 (STAR Methods).

(D) Flow cytometry of T cells isolated from CNS at d15.

(E–I) Effects of genetic perturbation of SAT1.

(E) Abundance of metabolites in differentiated WT or $SAT1^{-/-}$ T cells.

(F–I) EAE was induced in WT and $SAT1^{fl/fl}CD4^{cre}$ mice.

(F) Clinical score (left) and histological score (right) showing the number of CNS infiltrates.

(G and H) Antigen-specific response of cells from dLN (d23) is analyzed by proliferation (G) and antigen-specific cytokine secretion by LEGENDplex (H).

(I) Flow cytometry of cells isolated from CNS at d15. Linear regression analysis (B, C, F, and G), two-way ANOVA (E) and Student's t test (D and I) were used for statistical analysis.

See also Figure S7.

Even under this assumption, there remain an infinite number of feasible flux distributions that satisfy the preset biochemical constraints. Therefore, most studies assume that cells aim to optimize some metabolic function, usually biomass production (Damiani et al., 2019). However, although biomass maximization may successfully predict phenotypes in unicellular

organisms (Lewis et al., 2010), it is ill-suited for studying mammalian cells (Adler et al., 2019). To overcome this challenge, rather than optimizing a single metabolic objective, Compass optimizes a set of objective functions, each estimating the degree to which a cell's transcriptome supports carrying the maximal theoretical flux through a given reaction. The result is a high dimensional representation of the cell's metabolic potential (one coordinate per reaction). A biological signal (e.g., differential reaction activity) can be detected despite the high-dimension owing to the statistical power afforded by the large number of cells in a typical scRNA-seq dataset. Nonetheless, there is no inherent limitation preventing one from applying Compass to study bulk (i.e., non-single-cell) transcriptomic data.

Compass correctly predicted the role of aerobic glycolysis in the induction of pathogenic Th17 and the role of beta-oxidation in the induction of pro-regulatory Th17, mirroring previous findings in comparisons of Th17 to Treg. Compass also predicted novel metabolic targets that were associated with Th17 pathogenicity, one of which was the polyamine pathway. We investigated the metabolic circuitry centered around the polyamine pathway, and demonstrated its critical role in promoting pathogenicity and restricting a Treg-like program in Th17 cells. Because of reciprocal generation of Th17/Treg cells, the effects observed with the inhibition of polyamine pathway may be unique to diseases where Th17 cells are the effector cells. The significance of the polyamine pathway in autoimmunity contexts is further supported by anecdotal data that polyamine levels are increased in several autoimmune diseases (Hsu et al., 1994; Karouzakis et al., 2012) and it is thought that aberrant polyamine metabolism contributes to autoantigen stabilization (Brooks, 2013). Here, we present a mechanism through which the polyamine pathway can regulate epigenome and thereby Th17/Treg balance and impact development of autoimmunity. We showed that DFMO, which inhibits a key step of polyamine synthesis, substantially alters the Th17 effector profile. Because DFMO is a well-tolerated, Food and Drug Administration (FDA)-approved drug (Casero et al., 2018), there might be grounds for drug repurposing of DFMO for use in immune disorders.

Limitations of the study

Compass is subject to the limitations of static FBA. The Recon2 metabolic network is incomplete (e.g., lacks annotation of enzyme moonlighting functions) and pertains to a generalized human cell. Consequently, the current version of Compass does not consider the differences between human and mouse metabolism or tissue-specificity of the metabolic network. The algorithm makes the simplifying assumption of metabolic steady state and heuristically aggregates expression of multiple genes that are linked to a reaction. The inference of metabolic programs based on transcriptomes does not consider post-transcriptional and post-translational regulation, which could be particularly important for metabolic adaptations on short timescales. Last, the metabolic state of a cell depends on the nutrients available in its environment, which are often poorly characterized. Here, our computations assume an environment rich with nutrients, which accords with the studied *in vitro* growth media. A more accurate representation of the cellular environment should increase the algorithm's predictive capabilities.

Concerning polyamine metabolism, chemical inhibitions of several target enzymes led to similar effects on Th17 cells, but genetic deletions of ODC1 and SAT1 did not produce identical results. Although both ODC1 and SAT1 deletion promoted Foxp3 expression, ODC1, but not SAT1, suppressed Th17 cytokines *in vitro* (Figure 5I and data not shown). Further studies are necessary to understand the mechanistic roles and reciprocal regulation between the enzymes of the polyamine pathway *in vivo*.

STAR★METHODS

Detailed methods are provided in the online version of this paper and include the following:

- KEY RESOURCES TABLE
- RESOURCE AVAILABILITY
  - Lead contact
  - Materials availability
  - Data and code availability
- EXPERIMENTAL MODEL AND SUBJECT DETAILS
  - T cell differentiation culture
  - Mice
  - Experimental Autoimmune Encephalomyelitis (EAE)
- METHOD DETAILS
  - Flow cytometry
  - Seahorse assay
  - Inhibitors and metabolites
  - qPCR
  - Polyamine ELISA
  - Legendplex
  - RNA-Seq
  - LC/MS metabolomics and carbon tracing
  - Downstream analysis of Compass scores
  - Transcriptomic signatures
  - ATAC-Seq
  - Brief review of GSMM definitions
  - The Compass algorithm in detail
- QUANTIFICATION AND STATISTICAL ANALYSIS
  - Statistical Analysis of non-sequencing data

SUPPLEMENTAL INFORMATION

Supplemental information can be found online at https://doi.org/10.1016/j.cell.2021.05.045.

ACKNOWLEDGMENTS

We thank Eytan Ruppin and Michael B. Cole for fruitful discussions and Christina Usher for artwork. N.Y. and A.W. were supported by the Chan Zuckerberg Biohub and by the National Institute of Mental Health (NIMH) (NIH5U19MH114821). C.W. is a Medicine by Design Investigator supported by Canada First Research Excellence Fund. This work was supported by grants from the NIH (RO1NS30843, R01AI144166, R01NS045937, P01AI073748, P01AI039671, and P01AI056299 to V.K.K.) and by a Career Transitional Fellowship and faculty phase grant (TA-1605-08590 to C.W.) from the National

Multiple Sclerosis Society. J.F. was supported by a Max Kade fellowship awarded by the Austrian Academy of Science (ÖAW).

AUTHOR CONTRIBUTIONS

A.W., C.W., A.R., V.K.K., and N.Y. conceived and designed the study. A.W., D.D.T., and N.Y. designed the algorithm and performed computational analyses, B.S. aided in software development. C.W. conceived, designed, performed, and analyzed most experiments, with significant contributions by V.K.K., J.A.-P., K.P., and C.C. in LC/MS metabolomics and J.F. and S.Z. in inhibitor experiments. J.K. analyzed ATAC-seq datasets. E.C. generated most sequencing libraries. P.T. and V.S. provided help with ATAC-seq experiments. P.T. and A.S. optimized ATAC-seq protocol with input from A.R. R.S. performed histological analysis of EAE experiments. E.A.-G., L.B., and V.P.D. provided further experimental and analytical assistance. N.R.-H. and M.H. provided Seahorse assay support. D.P., E.P., and M.S. provided critical materials. V.K.K., N.Y., and C.W. supervised the study. A.W., C.W., V.K.K., and N.Y. wrote the manuscript with contributions from all authors. All authors read and approved the final manuscript.

DECLARATION OF INTERESTS

V.K.K. has an ownership interest and is a member of the SAB for Tizona Therapeutics and is a co-founder of and has an ownership interest in Celsius Therapeutics. V.K.K. is an inventor on patents related to Th17 cells and immunometabolism. V.K.K.'s interests were reviewed and managed by the Brigham and Women's Hospital and Partners Healthcare in accordance with their conflict of interest policies. N.Y. is an advisor for and/or has equity in Cellarity, Celsius Therapeutics, and Rheos Medicines. A.R. is a co-founder and equity holder of Celsius Therapeutics, an equity holder in Immunitas, and was a SAB member of ThermoFisher Scientific, Syros Pharmaceuticals, Neogene Therapeutics, and Asimov until July 31, 2020. From August 1, 2020, A.R. is an employee of Genentech. A.W., C.W., J.F., A.R., V.K.K., and N.Y. are co-inventors on a provisional patent application directed to inventions relating to methods for modulating metabolic regulators of T cell pathogenicity as described in this manuscript, filed by The Broad Institute, Brigham and Women's Hospital, and the Regents of California. All other authors declare no competing interests.

Received: January 3, 2020
Revised: February 15, 2021
Accepted: May 27, 2021
Published: July 2, 2021

REFERENCES

Adler, M., Korem Kohanim, Y., Tendler, A., Mayo, A., and Alon, U. (2019). Continuum of Gene-Expression Profiles Provides Spatial Division of Labor within a Differentiated Cell Type. Cell Syst. *8*, 43–52.e5.

Awasthi, A., Riol-Blanco, L., Jäger, A., Korn, T., Pot, C., Galileos, G., Bettelli, E., Kuchroo, V.K., and Oukka, M. (2009). Cutting edge: IL-23 receptor gfp reporter mice reveal distinct populations of IL-17-producing cells. J. Immunol. *182*, 5904–5908.

Baran, Y., Bercovich, A., Sebe-Pedros, A., Lubling, Y., Giladi, A., Chomsky, E., Meir, Z., Hoichman, M., Lifshitz, A., and Tanay, A. (2019). MetaCell: analysis of single-cell RNA-seq data using K-nn graph partitions. Genome Biol. *20*, 206.

Barbi, J., Pardoll, D., and Pan, F. (2013). Metabolic control of the Treg/Th17 axis. Immunol. Rev. *252*, 52–77.

Bauer, E., and Thiele, I. (2018). From Network Analysis to Functional Metabolic Modeling of the Human Gut Microbiota. mSystems *3*, 3.

Becker, S.A., and Palsson, B.O. (2008). Context-specific metabolic networks are consistent with experiments. PLoS Comput. Biol. *4*, e1000082.

Berod, L., Friedrich, C., Nandan, A., Freitag, J., Hagemann, S., Harmrolfs, K., Sandouk, A., Hesse, C., Castro, C.N., Bähre, H., et al. (2014). De novo fatty acid synthesis controls the fate between regulatory T and T helper 17 cells. Nat. Med. *20*, 1327–1333.

Bettelli, E., Carrier, Y., Gao, W., Korn, T., Strom, T.B., Oukka, M., Weiner, H.L., and Kuchroo, V.K. (2006). Reciprocal developmental pathways for the generation of pathogenic effector TH17 and regulatory T cells. Nature *441*, 235–238.

Bettelli, E., Korn, T., Oukka, M., and Kuchroo, V.K. (2008). Induction and effector functions of T(H)17 cells. Nature *453*, 1051–1057.

Bolger, A.M., Lohse, M., and Usadel, B. (2014). Trimmomatic: a flexible trimmer for Illumina sequence data. Bioinformatics *30*, 2114–2120.

Bordbar, A., Monk, J.M., King, Z.A., and Palsson, B.O. (2014). Constraint-based models predict metabolic and associated cellular functions. Nat. Rev. Genet. *15*, 107–120.

Bowlin, T.L., McKown, B.J., and Sunkara, P.S. (1987). The effect of alpha-difluoromethylornithine, an inhibitor of polyamine biosynthesis, on mitogen-induced interleukin 2 production. Immunopharmacology *13*, 143–147.

Bray, N.L., Pimentel, H., Melsted, P., and Pachter, L. (2016). Near-optimal probabilistic RNA-seq quantification. Nat. Biotechnol. *34*, 525–527.

Brooks, W.H. (2013). Increased polyamines alter chromatin and stabilize autoantigens in autoimmune diseases. Front. Immunol. *4*, 91.

Buck, M.D., Sowell, R.T., Kaech, S.M., and Pearce, E.L. (2017). Metabolic Instruction of Immunity. Cell *169*, 570–586.

Buenrostro, J.D., Giresi, P.G., Zaba, L.C., Chang, H.Y., and Greenleaf, W.J. (2013). Transposition of native chromatin for fast and sensitive epigenomic profiling of open chromatin, DNA-binding proteins and nucleosome position. Nat. Methods *10*, 1213–1218.

Casero, R.A., Jr., Murray Stewart, T., and Pegg, A.E. (2018). Polyamine metabolism and cancer: treatments, challenges and opportunities. Nat. Rev. Cancer *18*, 681–695.

Certo, M., Tsai, C.-H., Pucino, V., Ho, P.-C., and Mauro, C. (2021). Lactate modulation of immune responses in inflammatory versus tumour microenvironments. Nat. Rev. Immunol. *21*, 151–161.

Chapman, N.M., Boothby, M.R., and Chi, H. (2020). Metabolic coordination of T cell quiescence and activation. Nat. Rev. Immunol. *20*, 55–70.

Chung, Y., Chang, S.H., Martinez, G.J., Yang, X.O., Nurieva, R., Kang, H.S., Ma, L., Watowich, S.S., Jetten, A.M., Tian, Q., and Dong, C. (2009). Critical regulation of early Th17 cell differentiation by interleukin-1 signaling. Immunity *30*, 576–587.

Ciofani, M., Madar, A., Galan, C., Sellars, M., Mace, K., Pauli, F., Agarwal, A., Huang, W., Parkhurst, C.N., Muratet, M., et al. (2012). A validated regulatory network for Th17 cell specification. Cell *151*, 289–303.

Cole, M.B., Risso, D., Wagner, A., DeTomaso, D., Ngai, J., Purdom, E., Dudoit, S., and Yosef, N. (2019). Performance Assessment and Selection of Normalization Procedures for Single-Cell RNA-Seq. Cell Syst. *8*, 315–328.e8.

Conti, H.R., Peterson, A.C., Brane, L., Huppler, A.R., Hernández-Santos, N., Whibley, N., Garg, A.V., Simpson-Abelson, M.R., Gibson, G.A., Mamo, A.J., et al. (2014). Oral-resident natural Th17 cells and γδ T cells control opportunistic Candida albicans infections. J. Exp. Med. *211*, 2075–2084.

Corces, M.R., Buenrostro, J.D., Wu, B., Greenside, P.G., Chan, S.M., Koenig, J.L., Snyder, M.P., Pritchard, J.K., Kundaje, A., Greenleaf, W.J., et al. (2016). Lineage-specific and single-cell chromatin accessibility charts human hematopoiesis and leukemia evolution. Nat. Genet. *48*, 1193–1203.

Cua, D.J., Sherlock, J., Chen, Y., Murphy, C.A., Joyce, B., Seymour, B., Lucian, L., To, W., Kwan, S., Churakova, T., et al. (2003). Interleukin-23 rather than interleukin-12 is the critical cytokine for autoimmune inflammation of the brain. Nature *421*, 744–748.

Damiani, C., Maspero, D., Di Filippo, M., Colombo, R., Pescini, D., Graudenzi, A., Westerhoff, H.V., Alberghina, L., Vanoni, M., and Mauri, G. (2019). Integration of single-cell RNA-seq data into population models to characterize cancer metabolism. PLoS Comput. Biol. *15*, e1006733.

DeTomaso, D., Jones, M.G., Subramaniam, M., Ashuach, T., Ye, C.J., and Yosef, N. (2019). Functional interpretation of single cell similarity maps. Nat. Commun. *10*, 4376.

Diskin, C., Ryan, T.A.J., and O'Neill, L.A.J. (2021). Modification of Proteins by Metabolites in Immunity. Immunity *54*, 19–31.

Divakaruni, A.S., Hsieh, W.Y., Minarrieta, L., Duong, T.N., Kim, K.K.O., Desousa, B.R., Andreyev, A.Y., Bowman, C.E., Caradonna, K., Dranka, B.P., et al. (2018). Etomoxir Inhibits Macrophage Polarization by Disrupting CoA Homeostasis. Cell Metab. *28*, 490–503.e7.

Eisenstein, E.M., and Williams, C.B. (2009). The T(reg)/Th17 cell balance: a new paradigm for autoimmunity. Pediatr. Res. *65*, 26R–31R.

Elia, I., and Haigis, M.C. (2021). Metabolites and the tumour microenvironment: from cellular mechanisms to systemic metabolism. Nat. Metab. *3*, 21–32.

Fletcher, R.B., Das, D., Gadye, L., Street, K.N., Baudhuin, A., Wagner, A., Cole, M.B., Flores, Q., Choi, Y.G., Yosef, N., Purdom, E., Dudoit, S., Risso, D., Ngai, J., et al. (2017). Deconstructing Olfactory Stem Cell Trajectories at Single-Cell Resolution. Cell Stem Cell *20*, 817–830.e8.

Gaffen, S.L., Hernández-Santos, N., and Peterson, A.C. (2011). IL-17 signaling in host defense against Candida albicans. Immunol. Res. *50*, 181–187.

Gaublomme, J.T., Yosef, N., Lee, Y., Gertner, R.S., Yang, L.V., Wu, C., Pandolfi, P.P., Mak, T., Satija, R., Shalek, A.K., et al. (2015). Single-Cell Genomics Unveils Critical Regulators of Th17 Cell Pathogenicity. Cell *163*, 1400–1412.

Geltink, R.I.K., Kyle, R.L., and Pearce, E.L. (2018). Unraveling the Complex Interplay Between T Cell Metabolism and Function. Annu. Rev. Immunol. *36*, 461–488.

Gerriets, V.A., Kishton, R.J., Nichols, A.G., Macintyre, A.N., Inoue, M., Ilkayeva, O., Winter, P.S., Liu, X., Priyadharshini, B., Slawinska, M.E., et al. (2015). Metabolic programming and PDHK1 control CD4+ T cell subsets and inflammation. J. Clin. Invest. *125*, 194–207.

Ghoreschi, K., Laurence, A., Yang, X.-P., Tato, C.M., McGeachy, M.J., Konkel, J.E., Ramos, H.L., Wei, L., Davidson, T.S., Bouladoux, N., et al. (2010). Generation of pathogenic T(H)17 cells in the absence of TGF-β signalling. Nature *467*, 967–971.

Grant, C.E., Bailey, T.L., and Noble, W.S. (2011). FIMO: scanning for occurrences of a given motif. Bioinformatics *27*, 1017–1018.

Grün, D. (2020). Revealing dynamics of gene expression variability in cell state space. Nat. Methods *17*, 45–49.

Guglani, L., and Khader, S.A. (2010). Th17 cytokines in mucosal immunity and inflammation. Curr. Opin. HIV AIDS *5*, 120–127.

Haghverdi, L., Lun, A.T.L., Morgan, M.D., and Marioni, J.C. (2018). Batch effects in single-cell RNA-sequencing data are corrected by matching mutual nearest neighbors. Nat. Biotechnol. *36*, 421–427.

Heirendt, L., Arreckx, S., Pfau, T., Mendoza, S.N., Richelle, A., Heinken, A., Haraldsdóttir, H.S., Wachowiak, J., Keating, S.M., Vlasov, V., et al. (2019). Creation and analysis of biochemical constraint-based models using the COBRA Toolbox v.3.0. Nat. Protoc. *14*, 639–702.

Ho, P.-C., and Kaech, S.M. (2017). Reenergizing T cell anti-tumor immunity by harnessing immunometabolic checkpoints and machineries. Curr. Opin. Immunol. *46*, 38–44.

Hotamisligil, G.S. (2017). Foundations of Immunometabolism and Implications for Metabolic Health and Disease. Immunity *47*, 406–420.

Hsu, H.C., Seibold, J.R., and Thomas, T.J. (1994). Regulation of ornithine decarboxylase in the kidney of autoimmune mice with the lpr gene. Autoimmunity *19*, 253–264.

Huang, M., Wang, J., Torre, E., Dueck, H., Shaffer, S., Bonasio, R., Murray, J.I., Raj, A., Li, M., and Zhang, N.R. (2018). SAVER: gene expression recovery for single-cell RNA sequencing. Nat. Methods *15*, 539–542.

Jäger, A., Dardalhon, V., Sobel, R.A., Bettelli, E., and Kuchroo, V.K. (2009). Th1, Th17, and Th9 effector cells induce experimental autoimmune encephalomyelitis with different pathological phenotypes. J. Immunol. *183*, 7169–7177.

Jell, J., Merali, S., Hensen, M.L., Mazurchuk, R., Spernyak, J.A., Diegelman, P., Kisiel, N.D., Barrero, C., Deeb, K.K., Alhonen, L., et al. (2007). Genetically altered expression of spermidine/spermine N1-acetyltransferase affects fat metabolism in mice via acetyl-CoA. J. Biol. Chem. *282*, 8404–8413.

Jha, A.K., Huang, S.C.-C., Sergushichev, A., Lampropoulou, V., Ivanova, Y., Loginicheva, E., Chmielewski, K., Stewart, K.M., Ashall, J., Everts, B., et al. (2015). Network integration of parallel metabolic and transcriptional data reveals metabolic modules that regulate macrophage polarization. Immunity *42*, 419–430.

Johnson, M.O., Wolf, M.M., Madden, M.Z., Andrejeva, G., Sugiura, A., Contreras, D.C., Maseda, D., Liberti, M.V., Paz, K., Kishton, R.J., et al. (2018). Distinct Regulation of Th17 and Th1 Cell Differentiation by Glutaminase-Dependent Metabolism. Cell *175*, 1780–1795.e19.

Jung, J., Zeng, H., and Horng, T. (2019). Metabolism as a guiding force for immunity. Nat. Cell Biol. *21*, 85–93.

Kanehisa, M., Furumichi, M., Tanabe, M., Sato, Y., and Morishima, K. (2017). KEGG: new perspectives on genomes, pathways, diseases and drugs. Nucleic Acids Res. *45* (D1), D353–D361.

Karouzakis, E., Gay, R.E., Gay, S., and Neidhart, M. (2012). Increased recycling of polyamines is associated with global DNA hypomethylation in rheumatoid arthritis synovial fibroblasts. Arthritis Rheum. *64*, 1809–1817.

Khan, A., Fornes, O., Stigliani, A., Gheorghe, M., Castro-Mondragon, J.A., van der Lee, R., Bessy, A., Chèneby, J., Kulkarni, S.R., Tan, G., et al. (2018). JASPAR 2018: update of the open-access database of transcription factor binding profiles and its web framework. Nucleic Acids Res. *46* (D1), D1284.

Korn, T., Bettelli, E., Oukka, M., and Kuchroo, V.K. (2009). IL-17 and Th17 Cells. Annu. Rev. Immunol. *27*, 485–517.

Langmead, B., and Salzberg, S.L. (2012). Fast gapped-read alignment with Bowtie 2. Nat. Methods *9*, 357–359.

Law, C.W., Chen, Y., Shi, W., and Smyth, G.K. (2014). voom: Precision weights unlock linear model analysis tools for RNA-seq read counts. Genome Biol. *15*, R29.

Lee, Y., Awasthi, A., Yosef, N., Quintana, F.J., Xiao, S., Peters, A., Wu, C., Kleinewietfeld, M., Kunder, S., Hafler, D.A., et al. (2012). Induction and molecular signature of pathogenic TH17 cells. Nat. Immunol. *13*, 991–999.

Lee, Y., Collins, M., and Kuchroo, V.K. (2014). Unexpected targets and triggers of autoimmunity. J. Clin. Immunol. *34* (*Suppl 1*), S56–S60.

Lesurf, R., Cotto, K.C., Wang, G., Griffith, M., Kasaian, K., Jones, S.J.M., Montgomery, S.B., and Griffith, O.L.; Open Regulatory Annotation Consortium (2016). ORegAnno 3.0: a community-driven resource for curated regulatory annotation. Nucleic Acids Res. *44* (D1), D126–D132.

Lewis, N.E., Hixson, K.K., Conrad, T.M., Lerman, J.A., Charusanti, P., Polpitiya, A.D., Adkins, J.N., Schramm, G., Purvine, S.O., Lopez-Ferrer, D., et al. (2010). Omic data from evolved E. coli are consistent with computed optimal growth from genome-scale models. Mol. Syst. Biol. *6*, 390.

Lewis, N.E., Nagarajan, H., and Palsson, B.O. (2012). Constraining the metabolic genotype-phenotype relationship using a phylogeny of in silico methods. Nat. Rev. Microbiol. *10*, 291–305.

Li, Q., Zou, J., Wang, M., Ding, X., Chepelev, I., Zhou, X., Zhao, W., Wei, G., Cui, J., Zhao, K., et al. (2014). Critical role of histone demethylase Jmjd3 in the regulation of CD4+ T-cell differentiation. Nat. Commun. *5*, 5780.

Liu, Z., Cao, W., Xu, L., Chen, X., Zhan, Y., Yang, Q., Liu, S., Chen, P., Jiang, Y., Sun, X., et al. (2015). The histone H3 lysine-27 demethylase Jmjd3 plays a critical role in specific regulation of Th17 cell differentiation. J. Mol. Cell Biol. *7*, 505–516.

Love, M.I., Huber, W., and Anders, S. (2014). Moderated estimation of fold change and dispersion for RNA-seq data with DESeq2. Genome Biol. *15*, 550.

Lun, A.T.L., Bach, K., and Marioni, J.C. (2016). Pooling across cells to normalize single-cell RNA sequencing data with many zero counts. Genome Biol. *17*, 75.

Makowski, L., Chaib, M., and Rathmell, J.C. (2020). Immunometabolism: From basic mechanisms to translation. Immunol. Rev. *295*, 5–14.

Mangan, P.R., Harrington, L.E., O'Quinn, D.B., Helms, W.S., Bullard, D.C., Elson, C.O., Hatton, R.D., Wahl, S.M., Schoeb, T.R., and Weaver, C.T. (2006). Transforming growth factor-beta induces development of the T(H)17 lineage. Nature *441*, 231–234.

McGeachy, M.J., and Cua, D.J. (2008). Th17 cell differentiation: the long and winding road. Immunity *28*, 445–453.

McGeachy, M.J., Bak-Jensen, K.S., Chen, Y., Tato, C.M., Blumenschein, W., McClanahan, T., and Cua, D.J. (2007). TGF-beta and IL-6 drive the production of IL-17 and IL-10 by T cells and restrain T(H)-17 cell-mediated pathology. Nat. Immunol. *8*, 1390–1397.

McGeachy, M.J., Chen, Y., Tato, C.M., Laurence, A., Joyce-Shaikh, B., Blumenschein, W.M., McClanahan, T.K., O'Shea, J.J., and Cua, D.J. (2009). The interleukin 23 receptor is essential for the terminal differentiation of interleukin 17-producing effector T helper cells in vivo. Nat. Immunol. *10*, 314–324.

McLean, C.Y., Bristor, D., Hiller, M., Clarke, S.L., Schaar, B.T., Lowe, C.B., Wenger, A.M., and Bejerano, G. (2010). GREAT improves functional interpretation of cis-regulatory regions. Nat. Biotechnol. *28*, 495–501.

Michalek, R.D., Gerriets, V.A., Jacobs, S.R., Macintyre, A.N., MacIver, N.J., Mason, E.F., Sullivan, S.A., Nichols, A.G., and Rathmell, J.C. (2011). Cutting edge: distinct glycolytic and lipid oxidative metabolic programs are essential for effector and regulatory CD4+ T cell subsets. J. Immunol. *186*, 3299–3303.

Mills, E., and O'Neill, L.A.J. (2014). Succinate: a metabolic signal in inflammation. Trends Cell Biol. *24*, 313–320.

Mills, E.L., Kelly, B., Logan, A., Costa, A.S.H., Varma, M., Bryant, C.E., Tourlomousis, P., Däbritz, J.H.M., Gottlieb, E., Latorre, I., et al. (2016). Succinate Dehydrogenase Supports Metabolic Repurposing of Mitochondria to Drive Inflammatory Macrophages. Cell *167*, 457–470.e13.

Miragaia, R.J., Gomes, T., Chomka, A., Jardine, L., Riedel, A., Hegazy, A.N., Whibley, N., Tucci, A., Chen, X., Lindeman, I., et al. (2019). Single-Cell Transcriptomics of Regulatory T Cells Reveals Trajectories of Tissue Adaptation. Immunity *50*, 493–504.e7.

Monk, J., Nogales, J., and Palsson, B.O. (2014). Optimizing genome-scale network reconstructions. Nat. Biotechnol. *32*, 447–452.

Mounce, B.C., Poirier, E.Z., Passoni, G., Simon-Loriere, E., Cesaro, T., Prot, M., Stapleford, K.A., Moratorio, G., Sakuntabhai, A., Levraud, J.P., and Vignuzzi, M. (2016). Interferon-Induced Spermidine-Spermine Acetyltransferase and Polyamine Depletion Restrict Zika and Chikungunya Viruses. Cell Host Microbe *20*, 167–177.

O'Brien, E.J., Monk, J.M., and Palsson, B.O. (2015). Using Genome-scale Models to Predict Biological Capabilities. Cell *161*, 971–987.

O'Neill, L.A.J., Kishton, R.J., and Rathmell, J. (2016). A guide to immunometabolism for immunologists. Nat. Rev. Immunol. *16*, 553–565.

Omenetti, S., and Pizarro, T.T. (2015). The Treg/Th17 Axis: A Dynamic Balance Regulated by the Gut Microbiome. Front. Immunol. *6*, 639.

Orth, J.D., Thiele, I., and Palsson, B.O. (2010). What is flux balance analysis? Nat. Biotechnol. *28*, 245–248.

Ouyang, W., Kolls, J.K., and Zheng, Y. (2008). The biological functions of T helper 17 cell effector cytokines in inflammation. Immunity *28*, 454–467.

Palsson, B.Ø. (2015). Systems Biology: Constraint-Based Reconstruction and Analysis (Cambridge University Press).

Pegg, A.E. (2008). Spermidine/spermine-N(1)-acetyltransferase: a key metabolic regulator. Am. J. Physiol. Endocrinol. Metab. *294*, E995–E1010.

Pompura, S.L., Wagner, A., Kitz, A., LaPerche, J., Yosef, N., Dominguez-Villar, M., and Hafler, D.A. (2021). Oleic acid restores suppressive defects in tissue-resident FOXP3 Tregs from patients with multiple sclerosis. J. Clin. Invest. *131*, e138519.

Pucino, V., Certo, M., Bulusu, V., Cucchi, D., Goldmann, K., Pontarini, E., Haas, R., Smith, J., Headland, S.E., Blighe, K., et al. (2019). Lactate Buildup at the Site of Chronic Inflammation Promotes Disease by Inducing $CD4^+$ T Cell Metabolic Rewiring. Cell Metab. *30*, 1055–1074.e8.

Puleston, D.J., Villa, M., and Pearce, E.L. (2017). Ancillary Activity: Beyond Core Metabolism in Immune Cells. Cell Metab. *26*, 131–141.

Raud, B., Roy, D.G., Divakaruni, A.S., Tarasenko, T.N., Franke, R., Ma, E.H., Samborska, B., Hsieh, W.Y., Wong, A.H., Stüve, P., et al. (2018). Etomoxir Actions on Regulatory and Memory T Cells Are Independent of Cpt1a-Mediated Fatty Acid Oxidation. Cell Metab. *28*, 504–515.e7.

Regev, A., Teichmann, S.A., Lander, E.S., Amit, I., Benoist, C., Birney, E., Bodenmiller, B., Campbell, P., Carninci, P., Clatworthy, M., et al.; Human Cell Atlas Meeting Participants (2017). The Human Cell Atlas. eLife *6*, e27041.

Ritchie, M.E., Phipson, B., Wu, D., Hu, Y., Law, C.W., Shi, W., and Smyth, G.K. (2015). limma powers differential expression analyses for RNA-sequencing and microarray studies. Nucleic Acids Res. *43*, e47.

Romani, L. (2011). Immunity to fungal infections. Nat. Rev. Immunol. *11*, 275–288.

Roy, D.G., Kaymak, I., Williams, K.S., Ma, E.H., and Jones, R.G. (2021). Immunometabolism in the Tumor Microenvironment. Annu. Rev. Cancer Biol. *5*, 137–159.

Russell, D.G., Huang, L., and VanderVen, B.C. (2019). Immunometabolism at the interface between macrophages and pathogens. Nat. Rev. Immunol. *19*, 291–304.

Schellenberger, J., Lewis, N.E., and Palsson, B.Ø. (2011). Elimination of thermodynamically infeasible loops in steady-state metabolic models. Biophys. J. *100*, 544–553.

Shi, L.Z., Wang, R., Huang, G., Vogel, P., Neale, G., Green, D.R., and Chi, H. (2011). HIF1alpha-dependent glycolytic pathway orchestrates a metabolic checkpoint for the differentiation of TH17 and Treg cells. J. Exp. Med. *208*, 1367–1376.

Shi, L., Jiang, Q., Bushkin, Y., Subbian, S., and Tyagi, S. (2019). Biphasic Dynamics of Macrophage Immunometabolism during *Mycobacterium tuberculosis* Infection. MBio *10*, e02550-18.

Shlomi, T., Cabili, M.N., Herrgård, M.J., Palsson, B.O., and Ruppin, E. (2008). Network-based prediction of human tissue-specific metabolism. Nat. Biotechnol. *26*, 1003–1010.

Siepel, A., Bejerano, G., Pedersen, J.S., Hinrichs, A.S., Hou, M., Rosenbloom, K., Clawson, H., Spieth, J., Hillier, L.W., Richards, S., et al. (2005). Evolutionarily conserved elements in vertebrate, insect, worm, and yeast genomes. Genome Res. *15*, 1034–1050.

Singer, M., Wang, C., Cong, L., Marjanovic, N.D., Kowalczyk, M.S., Zhang, H., Nyman, J., Sakuishi, K., Kurtulus, S., Gennert, D., et al. (2016). A Distinct Gene Module for Dysfunction Uncoupled from Activation in Tumor-Infiltrating T Cells. Cell *166*, 1500–1511e9.

Subramanian, A., Tamayo, P., Mootha, V.K., Mukherjee, S., Ebert, B.L., Gillette, M.A., Paulovich, A., Pomeroy, S.L., Golub, T.R., Lander, E.S., and Mesirov, J.P. (2005). Gene set enrichment analysis: a knowledge-based approach for interpreting genome-wide expression profiles. Proc. Natl. Acad. Sci. USA *102*, 15545–15550.

Sundrud, M.S., Koralov, S.B., Feuerer, M., Calado, D.P., Kozhaya, A.E., Rhule-Smith, A., Lefebvre, R.E., Unutmaz, D., Mazitschek, R., Waldner, H., et al. (2009). Halofuginone inhibits TH17 cell differentiation by activating the amino acid starvation response. Science *324*, 1334–1338.

Thiele, I., Swainston, N., Fleming, R.M.T., Hoppe, A., Sahoo, S., Aurich, M.K., Haraldsdottir, H., Mo, M.L., Rolfsson, O., Stobbe, M.D., et al. (2013). A community-driven global reconstruction of human metabolism. Nat. Biotechnol. *31*, 419–425.

van Dijk, D., Sharma, R., Nainys, J., Yim, K., Kathail, P., Carr, A.J., Burdziak, C., Moon, K.R., Chaffer, C.L., Pattabiraman, D., et al. (2018). Recovering Gene Interactions from Single-Cell Data Using Data Diffusion. Cell *174*, 716–729.e27.

Varanasi, S.K., Kumar, S.V., and Rouse, B.T. (2020). Determinants of Tissue-Specific Metabolic Adaptation of T Cells. Cell Metab. *32*, 908–919.

Varma, A., and Palsson, B.O. (1994). Metabolic Flux Balancing: Basic Concepts, Scientific and Practical Use. Nat. Biotechnol. *12*, 994–998.

Veldhoen, M., Hocking, R.J., Atkins, C.J., Locksley, R.M., and Stockinger, B. (2006). TGFbeta in the context of an inflammatory cytokine milieu supports de novo differentiation of IL-17-producing T cells. Immunity *24*, 179–189.

Wagner, A., Regev, A., and Yosef, N. (2016). Revealing the vectors of cellular identity with single-cell genomics. Nat. Biotechnol. *34*, 1145–1160.

Wang, C., Yosef, N., Gaublomme, J., Wu, C., Lee, Y., Clish, C.B., Kaminski, J., Xiao, S., Meyer Zu Horste, G., Pawlak, M., et al. (2015). CD5L/AIM Regulates

Lipid Biosynthesis and Restrains Th17 Cell Pathogenicity. Cell *163*, 1413–1427.

Xiao, S., Yosef, N., Yang, J., Wang, Y., Zhou, L., Zhu, C., Wu, C., Baloglu, E., Schmidt, D., Ramesh, R., et al. (2014). Small-molecule RORγt antagonists inhibit T helper 17 cell transcriptional network by divergent mechanisms. Immunity *40*, 477–489.

Yang, Y., Torchinsky, M.B., Gobert, M., Xiong, H., Xu, M., Linehan, J.L., Alonzo, F., Ng, C., Chen, A., Lin, X., et al. (2014). Focused specificity of intestinal TH17 cells towards commensal bacterial antigens. Nature *510*, 152–156.

Yosef, N., Shalek, A.K., Gaublomme, J.T., Jin, H., Lee, Y., Awasthi, A., Wu, C., Karwacz, K., Xiao, S., Jorgolli, M., et al. (2013). Dynamic regulatory network controlling TH17 cell differentiation. Nature *496*, 461–468.

Zhang, Y., Liu, T., Meyer, C.A., Eeckhoute, J., Johnson, D.S., Bernstein, B.E., Nusbaum, C., Myers, R.M., Brown, M., Li, W., and Liu, X.S. (2008). Model-based analysis of ChIP-Seq (MACS). Genome Biol. *9*, R137.

Zielinski, C.E., Mele, F., Aschenbrenner, D., Jarrossay, D., Ronchi, F., Gattorno, M., Monticelli, S., Lanzavecchia, A., and Sallusto, F. (2012). Pathogen-induced human TH17 cells produce IFN-γ or IL-10 and are regulated by IL-1β. Nature *484*, 514–518.

STAR★METHODS

KEY RESOURCES TABLE

REAGENT or RESOURCE	SOURCE	IDENTIFIER
Antibodies		
Foxp3	ebioscience	Cat# 12-5773-82; RRID:AB_465936
Rorgt	ebioscience	Cat# 12-6981-82; RRID: AB_10807092
IL17A	biolegend	Cat# 506922; RRID:AB_2125010
IL-2	BD	Cat# 560547; RRID:AB_1727544
T-bet	biolegend	Cat# 644814; RRID: AB_10901173
GMCSF	biolegend	Cat# 505404; RRID: AB_315380
Chemicals, peptides, and recombinant proteins		
Etomoxir sodium salt hydrate	Sigma-Aldrich	E1905-5MG
L-Carnitine hydrochloride	Sigma-Aldrich	C0283-5G
Antimycin	Sigma-Aldrich	A8674-25MG
Poly-D-Lysine	Thermo Fisher Scientific	A3890401
D-Glucose-$^{13}C_6$	Sigma-Aldrich	389374
Putrescine dihydrochloride	Sigma-Aldrich	P7505
L-Arginine-13C6 hydrochloride	Sigma-Aldrich	643440
L-Citrulline-5-^{13}C,5,5-d_2	Sigma-Aldrich	734187
Eflornithine hydrochloride hydrate	Selleckchem	S4582
Critical commercial assays		
legendplex	Biolegend	741044
Total Polyamine Assay Kit	BioVision	K475
Deposited data		
Bulk RNA-Seq and ATAC-Seq of DFMO and Jmjd3 cKO in Th17 and Treg	GEO	GEO: GSE164999
Smart-Seq dataset of Th17p and Th17n single cells	GEO	GEO: GSE74833
Experimental models: organisms/strains		
Mouse: Jmjd3$^{fl/fl}$; B6.Cg-*Kdm6b*$^{tm1.1Rbo}$/J	The Jackson Laboratory	029615
Mouse: Sat1$^{fl/fl}$	Dr. Manoocher Soleimani's lab	Sat1$^{fl/fl}$
Mouse: ODC1$^{fl/fl}$CD4^{cre}	Dr. Erika Pearce's lab	ODC1$^{fl/fl}$CD4^{cre}
Oligonucleotides		
Ass1 taqman probe	ThermoFisher Scientific	4331182 (Mm00711256_m1)
Odc1 taqman probe	ThermoFisher Scientific	4331182 (Mm02019269_g1)
Sat1 taqman probe	ThermoFisher Scientific	4351372 (Mm07296282_g1)
Software and algorithms		
Compass	Prof. Nir Yosef's lab Github page	https://github.com/YosefLab/Compass

RESOURCE AVAILABILITY

Lead contact

Please direct comments and requests for software or laboratory resources to Nir Yosef (niryosef@berkeley.edu).

Materials availability

There are no newly generated materials in this paper. SAT1fl/fl mice were obtained from Dr. Manoocher Soleimani under MTA and cannot be redistributed.

Data and code availability

Compass is open-source and free for academic use. A Github repository is available at https://github.com/YosefLab/Compass. Sequencing data used in this study has been deposited to GEO under accession GEO: GSE164999. The data published in Gaublomme et al. (2015) and Wang et al. (2015) and reanalyzed here was deposited as GEO: GSE74833.

EXPERIMENTAL MODEL AND SUBJECT DETAILS

T cell differentiation culture

Naive CD4+CD44-CD62L+CD25-T cells were sorted using BD FACSAria sorter and activated with plate-bound anti-CD3 (1μg/ml) and anti-CD28 antibodies (1μg/ml) in the presence of cytokines at a concentration of 0.5 10^6 cells/ml. For T cell differentiations the following combinations of cytokines were used: pathogenic Th17: 25ng/ml rmIL-6, 20ng/ml rmIL-1b (both Miltenyi Biotec) and 20ng/ml rmIL-23 (RD systems); non-pathogenic Th17: 25ng/ml rmIL-6 and 2ng/ml of rhTGFb1 (Miltenyi Biotec); iTreg: 2ng/ml of rhTGFb1; Th1: 20ng/ml rmIL-12 (RD systems); Th2: 20ng/ml rmIL-4 (Miltenyi Biotec). For differentiation experiments, cells were harvested at 68 hours for RNA analysis or ATAC-Seq and 72-96h for flow cytometry analysis and Seahorse assay.

Mice

C57BL/6 wild-type (WT) mice were obtained from Jackson Laboratory (Bar Harbor, ME). WT 2D2 transgenic mice were bred in house. SAT1flox mice were kindly provided by Dr. Manoocher Soleimani (University of Cincinnati), which we crossed to $CD4^{cre}$ to generate conditional T cell deletion of SAT1. $ODC1^{fl/fl}CD4^{cre}$ were gifted by Dr. Erika Pearce (Max Planck Institute). For experiments, mice were matched for sex and age, and most mice were 6–10 weeks old. Littermate WT or Cre^- mice were used as controls. All experiments were performed in accordance to the guidelines outlined by the Harvard Medical Area Standing Committee on Animals at the Harvard Medical School or the Brigham and Women's hospital Institutional Animal Care and Use Committees (Boston, MA).

Experimental Autoimmune Encephalomyelitis (EAE)

For adoptive transfer EAE, naive T cells (CD4+CD44-CD62L+CD25-) were isolated from 2D2 TCR-transgenic mice and activated with anti-CD3 (1μg /ml) and anti-CD28 (1μg /ml) in the presence of differentiation cytokines for 68h. Cells were rested for 2 days and re-stimulated with plate-bound anti-CD3 (0.5μg/ml for pathogenic condition; 1μg/ml for non-pathogenic condition) and anti-CD28 (1μg/ml) for 2 days prior to transfer. Equal number (2 to 8 million) cells were transferred per mouse intravenously.

For active EAE immunization, MOG35-55 peptide was emulsified in complete freund adjuvant (CFA). Equivalent of 40μg MOG peptide was injected per mouse subcutaneously followed by pertussis toxin injection intravenously on day 0 and day 2 of immunization. Mice were treated with 0.5% DFMO in drinking water for 10 days as indicated. DFMO was replenished every third day.

EAE was scored as previously published (Jäger et al., 2009).

METHOD DETAILS

Flow cytometry

Intracellular cytokine staining was performed after incubation for 4-6h with Cell Stimulation cocktail plus Golgi transport inhibitors (Thermo Fisher Scientific) using the BD Cytofix/Cytoperm buffer set (BD Biosciences) per manufacturer's instructions. Transcription factor staining was performed using the Foxp3/Transcription Factor Staining Buffer Set (eBioscience). Proliferation was assessed by staining with CellTrace Violet (Thermo Fisher Scientific) per manufacturer's instructions. Apoptosis was assessed using Annexin V staining kit (BioLegend). Phosphorylation of proteins to determine cell signaling was performed with BD Phosflow buffer system (BD bioscience) as per manufacturer's instructions.

Seahorse assay

Seahorse assay was performed and seahorse media was prepared following manufacturer instructions (Agilent). Approximately 50,000 T cells were seeded per well in 96 well plate for seahorse assay and readout were normalized against cell count.

Inhibitors and metabolites

Inhibitors are added at the time of differentiation as follows: 100-200μM DFMO, 500μM trans-4-methylcyclohexylamine (MCHA, both Sigma), 500μM N-(3-Amino-propyl)cyclohexylamine (APCHA, Santa Cruz Biotechnology), 50μM diminazene aceturate (Dize, Cayman Chemical) with or without 2.5 mM putrescine (Sigma, P7505) as indicated.

qPCR

543369581089400RNA was isolated using RNeasy Plus Mini Kit (QIAGEN) and reverse transcribed to cDNA with iScript cDNA Synthesis Kit (Bio-Rad). Gene expression was analyzed by quantitative real-time PCR on a ViiA7 System (Thermo Fisher Scientific) using TaqMan Fast Advanced Master Mix (Thermo Fisher Scientific) with the following primer/probe sets:

- *Ass1* (Mm00711256 m1)

- *Odc1* (Mm02019269 g1)
- *Sat1* (Mm00485911 g1)
- *Srm* (Mm00726089 s1)
- *Sms* (Mm00786246 s1)
- *Il-17a* (Mm00439618 m1)
- *Il-17f* (Mm00521423 m1)
- *Foxp3* (Mm00475162 m1)
- *Tead1* (Mm00493507 m1)
- *Taz* (Mm00504978 m1)
- *Actb* (Applied Biosystems)

Expression values were calculated relative to *Actb* detected in the same sample by duplex qPCR.

Polyamine ELISA

Cell pellets of *in vitro* differentiated cells were frozen down and further processed with the Total Polyamine Assay Kit (BioVision Inc.) according to the manufacturer's instructions.

Legendplex

Cytokine concentrations in supernatants of *in vitro* cultures were analyzed by the LegendPlex Mouse Th Cytokine Panel (13-plex) (BioLegend) according to the manufacturer's instructions and analyzed on a FACS LSR II (BD Biosciences).

RNA-Seq

Bulk RNA sequencing

For population (bulk) RNA-seq, *in vitro* differentiated T cells were sorted for live cells and lysed with RLT Plus buffer and RNA was extracted using the RNeasy Plus Mini Kit (QIAGEN). Full-length RNA-Seq libraries were prepared as previously described (Singer et al., 2016) and paired-end sequenced (75 bp 2) with a 150 cycle Nextseq 500 high output V2 kit.

Smart-Seq single-cell RNA sequencing

Full experimental details are given in Gaublomme et al. (2015). Briefly, we sequenced CD4+ naive T cells 48hrs post polarization under the pathogenic (Th17p) or non-pathogenic (Th17n), ultimately retaining after quality tests 151 IL-17A/GFP+ Th17n cells, and 139 IL-17A/GFP+ Th17p cells. Unlike Gaublomme et al. (2015), in the present study we analyze only IL-17A/GFP+ sorted cells.

Estimation of transcript abundance from RNA libraries

We aligned single-cell SMART-Seq libraries with Bowtie2, quantified TPM gene expression with RSEM, and performed QC as we described in detail in a previous publication (Fletcher et al., 2017). This computational pipeline is a massively revised and updated version of the one originally used to analyze these libraries (Gaublomme et al., 2015). Batch effects and other nuisance factors were normalized with a model chosen empirically with SCONE (Cole et al., 2019). Bulk RNA-Seq were processed with a modified variant of the same pipeline, or with a Kallisto (Bray et al., 2016) pipeline. Both gave similar results.

Differential gene expression

For the Smart-Seq libraries, due the absence of UMIs in the dataset, differentially expressed genes were called through a linear model fitted to TPM values with the limma R package and with a mean-variance trend added to the empirical Bayes prior (Ritchie et al., 2015). For the bulk RNA libraries, differentially expressed genes were called with limma-trend or limma-voom (Law et al., 2014) depending on the variance of library sizes, as recommended in the limma package manual. Differentially expressed genes (DEGs) were decided by cutoffs of BH-adjusted $p \leq 0.05$ fold-change of at least 1.5 in absolute value.

Further bioinformatic analysis of RNA-Seq data

Bulk RNA libraries from DFMO- or vehicle-treated Th17p, Th17n, or Treg were studied with 3 replicates per condition for a total of 18 libraries as shown in Figure 6A. In all subsequent analyses, genes are considered differentially expressed by the cutoffs defined above.

The PCA shown in Figure 6A was computed on the set of 3,414 that were differentially expressed in comparisons of vehicle-treated Th17 (i.e., Th17n or Th17p) versus with iTreg, or vehicle-treated Th17p versus Th17n to focus it on the subspace of the transcriptome relevant to Th17 pathogenicity phenotypes.

Genes that are associated with a Th17 or Treg programs (orange and purple, respectively, in Figures 6B and 6C) were determined by differential expression test between bulk RNA libraries of vehicle-treated Th17 (i.e., Th17n or Th17p) one side and iTreg on the other. Similar results were obtained when the definition of the Th17 program (orange curve) and Treg programs was based on a comparison of only Th17n against iTreg cells.

A similar analysis was performed on the independent bulk-RNA dataset that involved Jmjd3 conditional knockout (Figures 6H and S6F). Th17 and Treg programs were defined based on differential expression of the vehicle-treated conditions from the dataset (i.e., not borrowed from the results of comparison within the previous dataset). Note, however, that no Th17p cells were included in this dataset, and therefore the Th17 program (orange curve) in Figures 6H and S6F is based on a comparison of Th17n against iTreg cells. Th17 and Treg-associated peaks in ATAC-Seq (Figure 6D) were similarly defined based on the ATAC-Seq dataset.

To further stratify genes into Th17-related programs (Figure S9A; based on the bulk RNA dataset shown in Figure 6A), we applied a heuristic based on four comparisons (all in vehicle-treated cells):

- Th17 (i.e., Th17n or Th17p) versus iTreg
- Th17p versus iTreg
- Th17n versus iTreg
- Th17p versus Th17n

The comparisons are decided based on differentially expression with the cutoffs defined above. A label is assigned to each gene as follows:

1. IF Th17 versus iTreg = = iTreg AND
Th17p versus iTreg = = iTreg AND
Th17n versus iTreg = = iTreg
THEN RETURN Treg (purple)
2. ELSE IF Th17 versus iTreg ≠ iTreg AND
Th17p versus iTreg = = Th17p AND
Th17p versus Th17n = = Th17p
THEN RETURN Th17p (magenta)
3. ELSE IF Th17 versus iTreg ≠ iTreg AND
Th17n versus iTreg = = Th17n AND
Th17p versus Th17n = = Th17n
THEN RETURN Th17n (green)
4. ELSE IF Th17 versus iTreg = = Th17
THEN RETURN Th17 (orange)
5. ELSE RETURN NS (gray)

The gene is associated with the Th17n, Th17p, general Th17, or Treg program by the returned label.

LC/MS metabolomics and carbon tracing

Assays

For untargeted metabolomics, Th17 cells were differentiated as described. Culture media were snap frozen. Cells were harvested at 96h. 1 10^6 cells per sample were snap frozen and extracted in either 80% methanol (for fatty acids and oxylipids) or isopropanol (for polar and nonpolar lipids). Two liquid chromatography tandem mass spectrometry (LC-MS) methods were used to measure fatty acids and lipids in cell extracts.

For carbon tracing experiments Th17 cells were differentiated as described. At 68hrs, cells were washed and cultured in media supplemented with 8mM [U-13C]-glucose for 15min or 3hrs. Alternatively, at 68hrs, cells were washed and cultured in media supplemented with arginine (^{13}C6, Sigma, Cat 643440) or aspartic acid (^{13}C4, Sigma, Cat 604852) for 1, 5 and 24 hours.

Statistical analysis

Differentially abundant metabolites were found with Student's t test and a significance threshold of BH-adjusted $p < 0.1$.

To find metabolites with differential 13C relative abundance, we computed the ratio $y_{i,j}$ of 13C out of the total carbon contents for each metabolite i in sample j. Let $|C_i|$ be the number of carbon atoms in metabolite i, and let $x_{c,i,j}$ be the measured signal of metabolite i in sample j (subsequent to all normalization and QC procedures) in which there are exactly c 13C atoms. We define the 13C/C ratio:

$$y_{ij} = \frac{\sum_{t=0}^{|C_i|} t \cdot x_{t,i,j}}{|C_i| \cdot \sum_{t=0}^{|C_i|} x_{t,i,j}}$$

Downstream analysis of Compass scores

Core metabolic reactions and meta-reactions

In this work, we define we core metabolism based on reaction metadata included in the Recon2 database. Recon2 assigns a confidence score to each reaction based on the level of evidence supporting it between 1 (no evidence) and 4 (biochemical evidence), with 0 denoting reactions whose confidence was not evaluated. Since pathways generally considered part of primary metabolism are also the best studied ones, we define a reaction as belonging to core metabolism if (a) its Recon2 confidence is either 0 or 4; *and* (b) it is annotated with an EC (Enzyme Commission) number. We chose to label reactions with unevaluated confidence (i.e., Recon2 confidence score of 0) as part of core metabolism because some of them were found to be key reactions in primary metabolic pathways based on manual correction. Our definition of core metabolism is equivalent to taking the set of all metabolic reactions in Recon2, but

excluding reactions that either don't have an annotated EC number or for which the Recon2 curators explicitly specified they do not have direct biochemical support. We define a meta-reaction as belonging to core metabolism if it contains at least one core reaction. Core pathways are defined as Recon2 subsystems that have at least 3 core reactions. Metabolic genes are defined as the set of genes annotated in Recon2.

Finding reactions with differential potential activity

To test for differential potential-activity of reactions based on Compass predictions, we computed for each meta-reaction M the Wilcoxon's rank sum between the Compass scores of M in the two populations of interest (here, Th17p and Th17n). Effect size were further assessed with Cohen's d statistic, defined as the difference between the sample means over the pooled sample standard deviation. Let n_1, x_1, s_1 be the number of observations in population 1, and the sample mean and standard deviation of their scores in a given meta-reaction, respectively (with a similar notation for population 2). Then

$$d = \frac{\left(\overline{x_1} - \overline{x_1}\right)}{s}$$

with

$$s = \sqrt{\frac{(n_1 - 1)s_1^2 + (n_2 - 1)s_2^2}{n_1 + n_2 - 2}}$$

The resulting p values are adjusted with the Benjamini-Hochberg (BH) method. Note that so far, the computation was done for meta-reactions. We assigned all reactions $r \in M$ the Cohen's d and Wilcoxon's p value that were computed for M . We call a reaction differentially active if its adjusted p is smaller than 0.1. The computation was done on all reactions in the network (namely, both core and non-core reactions).

Manual curation of central carbon predictions

We manually curated the significant predictions of the central carbon metabolism pathways discussed in the manuscript (glycolysis, TCA cycle, and fatty acid synthesis/oxidation). Recon2 takes account of metabolite localization, and reactions may be functional in more than one cellular compartment. For every reaction, we picked the prediction corresponding to the pertinent cellular compartment (here, cytosol or mitochondria, as shown in Figure 4A). Note that Compass operates independently on the forward and backward directions of every reaction, and that the direction is denoted in the pathway diagrams of this manuscript.

Transcriptomic signatures

Th17 pathogenicity

We used a transcriptomic signature that we have previously shown to capture a Th17 cell's pathogenic capacity (Gaublomme et al., 2015; Wang et al., 2015). Briefly, for each cell compute the average z-scored expression (log(1 +TPM)) of pro-pathogenic markers (CASP1, CCL3, CCL4, CCL5, CSF2, CXCL3, GZMB, ICOS, IL22, IL7R, LAG3, LGALS3, LRMP, STAT4, TBX21) and pro-regulatory markers (AHR, IKZF3, IL10, IL1RN, IL6ST, IL9, MAF), with the latter group multiplied by −1.

A compendium of T cell state signatures

A compendium of T cell state transcriptomic signatures was described in Gaublomme et al. (2015). Every signature consists of two gene subsets: a set of positively associated genes and an optionally empty set of negatively associated genes. A scalar signature value is computed for every cell based on its transcriptome profile as described above for pathogenicity. Signatures that are based on KEGG (Kanehisa et al., 2017) pathways or similar resources are constructed by defining the set of positively-associated genes as the ones belonging to the pathway and defining the set of negatively-associated genes as an empty set.

Total metabolic activity of a cell

We defined the total metabolic activity of a cell as the sum expression of metabolic enzyme coding genes over the sum expression of all protein coding genes in log-scale TPM (transcripts per million) units. We computed the partial correlation between this quantity and cell PC1 coordinates, while controlling for the sum expression of all protein coding genes in the cells (the aforementioned divisor) to verify the correlation does not arise from the ratio of protein-coding to non-protein coding RNA in the RNA libraries. The correlation was more significant when not controlling for the covariate (Pearson rho = 0.56, $p < 3 \cdot 10^{-16}$).

Late-stage Th17 differentiation

We defined a transcriptomic signature for late-stage differentiation of Th17 cells based on microarray data from Yosef et al. (2013). We assigned microarrays into three differentiation stages as described in that paper into early (up to 4h), intermediate (6-16h) and late (20-72h) and fitted with the limma R package a linear model for the discrete 3-level stage covariate. We called differentially expressed genes (BH-adjusted $p < 0.05$ and log2 fold-change ≥ 3) and used them to define a transcriptomic signature as described above.

ATAC-Seq

Library preparation

For population ATAC-Seq, *in vitro* differentiated T cells were sorted for live cells and stored in Bambanker freezing media (Thermo Fisher Scientific) at −80 °C until further processing. Prior to library preparation, cells were thawed at 37 °C and washed with PBS. For

ATAC-Seq, cell pellets were lysed and tagmented in 1X TD Buffer, 0.2μl TDE1 (Illumina), 0.01% digitonin, and 0.3X PBS in 40μl reaction volume following the protocol described in Corces et al. (2016). Transposition reactions were incubated at 37for 30 min at 300 rpm. The DNA was purified from the reaction using a MinElute PCR purification kit (QIAGEN). The whole resulting product was then PCR-amplified using indexed primers with NEBNext High-Fidelity 2X PCR Master Mix (NEB). First, we performed 5 cycles of pre-amplification. We sampled 10% of the pre-amplification reaction for SYBR Green quantitative PCR to assess the number of additional cycles needed for final amplification. After purifying the final library with the MinElute PCR purification kit (QIAGEN), the library was quantified for sequencing using qPCR and a Qubit dsDNA HS Assay kit (Invitrogen). Libraries were sequenced on an Illumina NextSeq 550 system with paired-end reads of 37 base pairs in length.

Alignment of ATAC-Seq and peak calling

All ATAC-Seq reads were trimmed using Trimmomatic (Bolger et al., 2014) to remove primer and low-quality bases. Reads smaller than 36bp were dropped. Reads were then passed to FastQC [https://www.bioinformatics.babraham.ac.uk/projects/fastqc/] to check the quality of the trimmed reads. The paired-end reads were then aligned to the mm10 reference genome using bowtie2 (Langmead and Salzberg, 2012), allowing maximum insert sizes of 2000 bp, with the–no-mixed and–no-discordant parameters added. Reads with a mapping quality (MAPQ) below 30 were removed. Duplicates were removed with PicardTools, and the reads mapping to the blacklist regions and mitochondrial DNA were also removed. Reads mapping to the positive strand were moved +4bp, and reads mapping to the negative strand were moved −5bp following the procedure outlined in Buenrostro et al. (2013) to account for the binding of the Tn5 transposase.

Peaks were called using macs2 on the aligned fragments (Zhang et al., 2008) with a qvalue cutoff of 0.001 and overlapping peaks among replicates were merged.

Tests of differential accessibility

Differential accessibility was assessed using DESeq2 (Love et al., 2014) with a matrix of peaks (merging all samples) by samples. Similar to common practice in the analysis of differential gene expression, our analysis of differential accessibility was conducted using the number of observed Tn5 cuts (i.e., number of reads).

Peaks that are associated with a Th17 or Treg programs (orange and purple, respectively, in Figure 6D) were determined by differential accessibility test between libraries of vehicle-treated (water) Th17n and Th17p on one side (unpublished dataset) and Treg on the other with BH-adjusted $p \leq 0.05$ and absolute value of log2 fold-change of at least 1.

Reprocessing of published ChIP-Seq data

ChIP-Seq Peaks from Xiao et al. (2014) were transferred from mm9 to mm10 using the UCSC liftOver tool. ChIP-Seq replicates from Ciofani et al. (2012) were downloaded and were trimmed using Trimmomatic (Bolger et al., 2014) to remove primer and low-quality bases. Reads were then passed to FastQC [http://www.bioinformatics.babraham.ac.uk/projects/fastqc/] to check the quality of the trimmed reads. These single-end reads were then aligned to the mm10 reference genome using bowtie2 (Langmead and Salzberg, 2012) allowing maximum insert sizes of 2000 bp, with the–no-mixed and–no-discordant parameters added. Reads with a mapping quality (MAPQ) below 30 were removed. Duplicates were removed with PicardTools, and the reads mapping to the blacklist regions and mitochondrial DNA were also removed.

ChIP-Seq peaks were called in each replicate, versus a control sample, using macs2 (Zhang et al., 2008) with a qvalue cutoff of 0.05.

Enrichment of motifs and ChIP-Seq peaks

Peaks were considered differentially accessible if they had a BH-adjusted $p < 0.05$. We calculated fold enrichment of various genomic features in these peaks (described below) versus a background set of peaks. q-values were estimated using q-value R package [https://github.com/jdstorey/qvalue].

Motifs and annotation tracks

PWM's for motifs were downloaded from the 2018 release of JASPAR (Khan et al., 2018). We used FIMO (Grant et al., 2011) to identify motifs in mm10, and applied the default threshold of 10^{-4}. We also included the following genomic features from the UCSC Genome Browser [http://genome.ucsc.edu]: the ORegAnno database (Lesurf et al., 2016), conserved regions annotated by the PHAST package (Siepel et al., 2005), and repeat regions annotated by RepeatMasker [http://www.repeatmasker.org].

GREAT pathways and genes

Loci were associated with genes and pathways using GREAT (McLean et al., 2010), submitted with the rGREAT R package [https://github.com/jokergoo/rGREAT]. We retrieved pathways found in the MSigDB Immunologic Signatures, MSigDB Pathways, and GO Biological Processes databases.

Brief review of GSMM definitions

We provide a brief review of key concepts, for a comprehensive review of genome-scale metabolic modeling see Bauer and Thiele (2018), Bordbar et al. (2014), Heirendt et al. (2019), Lewis et al. (2012), O'Brien et al. (2015), Orth et al. (2010) and Palsson (2015).

Stoichiometric matrix (S)

A stoichiometric matrix *S* describes the set of possible metabolic reactions in the system. Its rows correspond to metabolites, columns to reactions, and entries hold the stoichiometric coefficients of the reactions available to the cells.

Metabolic flux (v)

A metabolic flux is the instantaneous rate in which a chemical reaction occurs, and measured in units of mol X gDW^{-1} X hr^{-1}, with gDW denoting gram dry weight. Let x be metabolite concentrations in the system (as a function of time t), and v be the metabolic fluxes (also called *flux distribution*). Then:

$$S \cdot v = \frac{dx}{dt}$$

Compass belongs to the family of static FBA algorithms (Orth et al., 2010), which assumes metabolic steady-state, i.e.

$$S \cdot v = 0$$

Equivalently, we limit the space of feasible flux distributions to $\ker(S)$.

Genome-scale metabolic model (GSMM)

Compass leverages prior knowledge about the metabolic network of the cells in question in the form of a Genome-Scale Metabolic Model (GSMM), which includes the following components (Heirendt et al., 2019; Monk et al., 2014; O'Brien et al., 2015; Palsson, 2015):

- A stoichiometric matrix S
- Reactions are partitioned into cellular *compartments* representing membrane-enclosed space in which a biochemical reaction may take place, for example the cytosol, Golgi, or mitochondria.
- Metabolites are represented separately for each compartment. For example, cytosolic citrate and mitochondrial citrate correspond to two rows in S.
- Reactions may contain non-zero coefficients for metabolites located in different compartment to represent physiological transportation of metabolites across membranes. These reactions are called *Transport reactions*.
- The extracellular space is represented as an additional compartment.
- Reactions may have exactly one non-zero coefficient if the corresponding metabolite is located in the extracellular space. These reactions are called *exchange reactions* and used to import metabolites into or export them from the system. It is standard convention to assign -1 as the non-zero coefficient of exchange reactions.
- Upper and lower bounds on fluxes through the reactions corresponding to columns of S.
- Lower bounds of exchange reactions limit metabolite uptake and used to simulate constraints on nutrient availability. Note these are the lower, and not upper, bounds because the exchange coefficient is -1.
- A set if genes coding enzymes that catalyze reactions in the network
- Gene-to-reaction associations:
- Every reaction is associated with a boolean expression over gene literals and the $\{\vee, \wedge\}$ operators.
- Every gene is assigned a truth value based on its presence or absence in the cell's genome. A gene may be absent, for example, in a knockout genotype.
- The boolean expressions code the dependency of reactions on their catalyzing proteins. Usually, an OR relationship corresponds to isozymes, namely two enzymes capable of catalyzing the same reaction, and AND relationship corresponds to enzyme complexes.

The Compass algorithm in detail

Notation

In the following sections we denote:

- n: number of cells (or RNA libraries).
- m: number of metabolic reactions in the GSMM.
- C: the set of cells in the data. ($|C| = n$).
- R: the set of metabolic reactions in the GSMM. ($|R| = m$).
- $rev(r)$: the reverse unidirectional reaction of reaction r, which has the same stoichiometry but proceeds in the opposite direction.
- g: number of genes in a given transcriptome dataset.
- S: the stoichiometric matrix defined in the GSMM, where rows represent metabolites, columns represent reactions, and entries are stoichiometric coefficients for the reactions comprising the metabolic network. Reactions for uptake and secretion of a metabolite are encoded as having only a coefficient of 1 and -1 in the metabolite's row entry, respectively, and 0 otherwise.

For a matrix $M = (m_{i,j})$ and a function $f: \mathbb{R} \rightarrow \mathbb{R}$ we use $f(M)$ to denote (where the intention is obvious from the context) the respective point-wise transformation, namely $f(M) := (f(m_{i,j}))$.

Transcriptome-agnostic preparatory step

For a given GSMM (here, Recon2), we run once a preparatory step that does not depend on transcriptome data and cache the results (Algorithm 1).

center102108000Constraint *(i)* constrains the system to steady state (Varma and Palsson, 1994). Constraint *(ii)* is interpreted as $\forall i$: $\alpha_i \leq v_i \leq \beta_i$ and encodes directionality and capacity limits for reactions, including uptake and secretion limits. Constraint *(iii)* ensures that when evaluating the maximum flux for each reaction, its reverse reaction carries no flux to avoid the creation of a futile cycle. This does not prevent futile cycles longer than 2 edges, which can be avoided only by more time-consuming computations (Schellenberger et al., 2011).

Algorithm 1: Find maximal reaction fluxes

input : GSMM
output: maximal flux v_r^{opt} that every reaction r can carry

1 **foreach** $r \in \mathcal{R}$ **do**
2

$$v_r^{opt} := \underset{v \in \mathbb{R}^m}{\text{maximize}}\ v_r$$
$$\text{s.t.}$$
$$(i) \quad S \cdot v = 0$$
$$(ii) \quad \alpha \leq v \leq \beta$$
$$(iii) \quad v_{rev(r)} = 0$$

3 **end**

Note that the GSMM may contain blocked reactions ($v^{opt} = 0$) that can be excluded from the next steps to speed the computation.

From gene expression to reaction expression

By reaction expression, we denote a matrix $\{R(G)\}_{m \times n}$ that is conceptually similar to the gene expression matrix $G_{g \times n}$. The columns are the same RNA libraries (e.g., cells) as in $\{G\}$, but rows represent single metabolic reactions rather than transcripts. An entry $R_{r,j}$ in the matrix $R(G)$ is a quantitative proxy for the activity of reaction r in cell j. We omit the dependence on gene expression matrix and denote simply R when G is obvious from the context.

The reaction expression matrix is created by using the boolean gene-to-reaction mapping included in the GSMM, similar to the approach taken by (Becker and Palsson, 2008; Shlomi et al., 2008) Let $G = x_{i,j}$ and consider a particular reaction r in a particular cell j. If a single gene with linear-scale expression x is associated with r, then the reaction's expression will be $R_{r,j} = \log2(x + 1)$. If no genes are associated with r then $R_{r,j} = 0$.

If the reaction is associated with more than one gene, then this association is expressed as a boolean relationship. For example, two genes which encode different subunits of a reaction's enzyme are associated using an AND relationship as both are required to be expressed for the reaction to be catalyzed. Alternately, if multiple enzymes can catalyze a reaction, the genes involved in each will be associated via an OR relationship. For reactions associated with multiple genes in this manner, the boolean expression is evaluated by taking the sum or the mean of linear-scale expression values x when genes are associated via an OR or AND relationship, respectively. This way, the full gene(s)-to-reaction associations is evaluated to arrive at a single summary expression value for each reaction in the GSMM.

Information sharing between single cells (smoothing)

To mitigate the sparseness and stochasticity of single-cell measurements, Compass allows for a degree of information-sharing between cells with similar transcriptional profiles. Given a gene expression G, we compute k-nearest neighbors (kNN) graph based Euclidean distances in reduced dimension, obtained by taking the top 20 principal components of G. The PCA is computed over all the genes in G, not only metabolic ones.

Let $R(G) = \{r_{i,j}\}$ and

$$w_{i,j} = \begin{cases} \frac{1}{k}, \text{ if cell } j \text{ is in the } k - \text{nearest} - \text{neighborhood of cell } i, \\ 0, \text{ otherwise} \end{cases}$$

Then $R^N(G) = \{r^N_{i,j}\}$ where

$$r^N_{i,j} = \sum_{c \in C} w_{j,c} r_{i,c}$$

Main algorithm

Compass transforms a gene expression matrix $\{G\}_{g \times n}$, where rows represent genes and columns represent RNA libraries (usually, single cells, although bulk RNA can also be used as discussed below) into a matrix $\{C\}_{m \times n}$ of scores where rows represent metabolic

reactions, columns are the same RNA libraries as in the gene expression, and an entry quantifies a proxy for potential reaction activity. More precisely, the entry quantifies the propensity of the cell to use that reaction.

The algorithm is summarized in (Algorithm 2). First, we convert the gene expression matrix $G_{g \times n}$ into a *reaction expression* matrix $R_{m \times n}$ which is parallel to the gene expression matrix, but with rows representing single metabolic reactions rather than transcripts. We convert R into a *penalty matrix* $P_{m \times n}$ by point-wise inversion. Whereas R represents gene expression support that a reaction is functional in the cell, P represents the lack thereof (which will be used in a linear program below). The computation of R and P occurs also for the neighborhood of each cell for to smooth results and mitigate single-cell technical noise. Then, we solve a linear program for every reaction r in every cell i to find the minimal resistance of cell i to carry maximal flux through r. Last, we scale the scores, which also entails negating them such that that larger scores will represent larger potential activities (instead of larger penalties, hence smaller potential activity). The final scores indicative of a cell's propensity to use a certain reaction. We interpret it as a proxy for the potential activity of the reaction in that cell.

In step 10 of Algorithm 2, a high penalty $yr_{,c}$ indicates that cell c is unlikely, judged by transcriptomic evidence, to use reaction r. Cells whose transcriptome are overall more aligned with an ability to carry flux through a reaction will be assigned a lower penalty $yr_{,c}$. With regards to the correctness of the step, recall that that the GSMM is unidirectional and therefore $\forall i.\ v_i > 0$.

Algorithm 2: Compass

input : Gene expression matrix $\{G\}_{g \times n}$
GSMM
Pre-computed maximal fluxes $\{v_r^{opt} : r \in \mathcal{R}\}$
output : Compass scores matrix $\{C\}_{m' \times n}$ $(m' \leq m)$
parameters: Smoothing parameter $\lambda \in [0, 1]$ (here, $\lambda = 0.25$)
Nearest neighbor parameter k (here, $k = 10$)
Optimality slack parameter $\omega \in [0, 1]$ (here, $\omega = 0.95$)
Penalty function $p(x)$ (here, $p(x) = 1/(1 + x)$)
Meta-reaction merging threshold $\rho \in [0, 1]$ (see below)

1 Compute with the procedures described above:
2 a reaction expression matrix $\{R(G)\}_{m \times n}$
3 a neighborhood reaction expression matrix $\{R^N(G)\}_{m \times n}$
4 Transform reaction expressions to penalties:
5

$$P := p(R(G))$$
$$P^N := p(R^N(G))$$

6 $\hat{P} := (1 - \lambda)P + \lambda P^N$
7 **foreach** $r \in \mathcal{R}, c \in \mathcal{C}$ **do**
8 Let $\hat{P}^{(c)} = \left(\hat{P}_{1,c}, \ldots, \hat{P}_{m,c}\right)$
9

$$y_{r,c} := \underset{v \in \mathbb{R}^m}{\textbf{minimize}}\ \hat{P}^{(c)} \cdot v$$
$$\textbf{s.t.}$$
$$(i) \quad S \cdot v = 0$$
$$(ii) \quad \alpha \leq v \leq \beta$$
$$(iii) \quad v_{rev(r)} = 0$$
$$(iv) \quad v_r \geq \omega \cdot v_r^{opt}$$

10 **end**
11 Let $C^{raw} = \{y_{r,c}\}_{m \times n}$
12 Compute meta-reaction scores $C^{meta-raw} = \{y'_{r,c}\}_{m'' \times n}$ $(m'' \leq m)$ as described below
13 Use Algorithm 3 to scale $C^{meta-raw}$ and obtain C
14 Remove constant rows from C, defined as rows in which the difference between largest and smallest score is less than $\varepsilon = 10^{-3}$
15 **return** C

Meta-reactions

Rows in the C^{raw} matrix that correspond to reactions that are topologically close in the metabolic network can be highly correlated. We therefore hierarchically cluster C^{raw} rows by Spearman distance. We call the resulting clusters meta-reactions and each represents a set of closely correlated metabolic reactions. Note that the division into meta-reactions is data-driven and does not rely on canonical metabolic pathway definitions. Therefore, the division is dataset-dependent — for example, two reactions might be closely correlated and clustered in the same meta-reaction in one cell type, but not in another.

After computing the hierarchical clusters over rows of C^{raw}, we merged leaves in which Spearman similarity (namely $1 - \rho$, with ρ being the Spearman correlation) by averaging the respective rows. In the present work, we used $\rho = 0.98$. We denote the row-merged matrix $\{C^{meta-raw}\}_{mXn}$.

Scaling raw compass scores

center88265000By definition, all entries in $C^{meta-raw}$ are non-negative. We scale it in Algorithm 3 (the min in the second step denotes matrix-wide minimal entry)

Algorithm generalization

One of the intuitions behind Compass is that the statistical power afforded by the number of observations (cells) in

Algorithm 3: Scale raw Compass scores

input : $C^{meta-raw}$
output : C
1 $C^{meta-raw} := -\log(1 + C^{meta-raw})$
2 $C := C^{meta-raw} - \min(C^{meta-raw})$
3 **return** C

single-cell RNA-Seq allows *increasing* dimensionality by computing a new feature set based on the gene expression data and the GSMM. Here, we used an intuitive set of objective functions — for each reaction in the network, we defined one objective function which is to maximize the flux it carries (recall that the network is unidirectional and therefore all reactions carry non-negative fluxes). This allows intuitive interpretation of the Compass scores as quantitative proxies to reaction activities. However, the algorithm can be generalized by using an arbitrary set of linear objective functions that pertain to cellular metabolism.

Scalability

For prohibitively large datasets, the number of cells (observations) can be reduced by partitioning the cells into small clusters and treating the average of each cluster as an observation in downstream analysis. Two implementations of this approach are *micropools* (DeTomaso et al., 2019) implemented in the VISION R package (https://github.com/YosefLab/VISION), and meta-cells (Baran et al., 2019) (https://tanaylab.github.io/metacell). No pooling was necessary for the analysis presented in this manuscript (i.e., the results are on a single cell level). If cell clusters are large enough, one may choose to skip the information-sharing procedure, which is equivalent to setting the parameter $\lambda = 0$ in Algorithm 2.

In addition, the number of reactions in the GSMM can be reduced as well by not executing Algorithm 2 on blocked reactions (Section 1.3) non-core reactions (Section 1.11.2), or reactions outside a predetermined set of metabolic pathways that are of interest. We note that we do not suggest excluding non-blocked reactions from the network altogether (which would result in neglecting their effects on reactions that are of interest), but rather only excluding them from the $R(G)$ matrices in Algorithm 2.

Metabolic network

We used the Recon2 GSMM (Thiele et al., 2013) which we transformed into a unidirectional network by replacing bidirectional reactions with the respective pair of unidirectional reactions. Consequently, flux values are always non-negative.

In silico *growth medium*

The results of flux balance analysis significantly depend on the nutrients made available to the GSMM, referred to as the *in silico* growth medium. Since exact medium composition is mostly unknown even for common *in vitro* protocols and *in vivo* models, we chose a rich *in silico* medium where all nutrients for which a transporter exits are made available in an unlimiting quantity.

Gene expression input

The main input is gene expression matrix G in which rows correspond to genes and columns to RNA libraries. We assume that G is (i) already normalized to remove batch and other nuisance effects; (ii) scaled to CPMs or TPMs. In the present work we used TPMs; *and* (iii) in linear (i.e., not log) scale.

Metabolic genes

Throughout this work, metabolic genes are defined as the set of genes annotated in Recon2. Note that Compass uses only the expression of metabolic genes and ignores other transcripts.

Running Compass on bulk (i.e., non-single-cell) inputs

The current manuscript presents the algorithm in the context of single cells, where Compass leverages the statistical power afforded by the large number of observations (cells). Nevertheless, there is no inherent limitation preventing one from applying Compass to study bulk (i.e., non-single-cell) transcriptomic data. In this case, we recommend disabling the information-sharing feature by setting *lambda* = 0 in Algorithm 2. There is also no limitation preventing one from applying Compass to non-RNA-Seq transcriptomic data, such as microarrays.

QUANTIFICATION AND STATISTICAL ANALYSIS

Statistical Analysis of non-sequencing data

Unless otherwise specified, the tests performed were two-tail Welch t tests using Prism software. P values were adjusted with the Bonferroni method for multiple comparisons where appropriate. P value less than 0.05 is considered significant ($p < 0.05$ = *; $p < 0.01$ = **; $p < 0.001$ = ***) unless otherwise indicated.

Supplemental figures

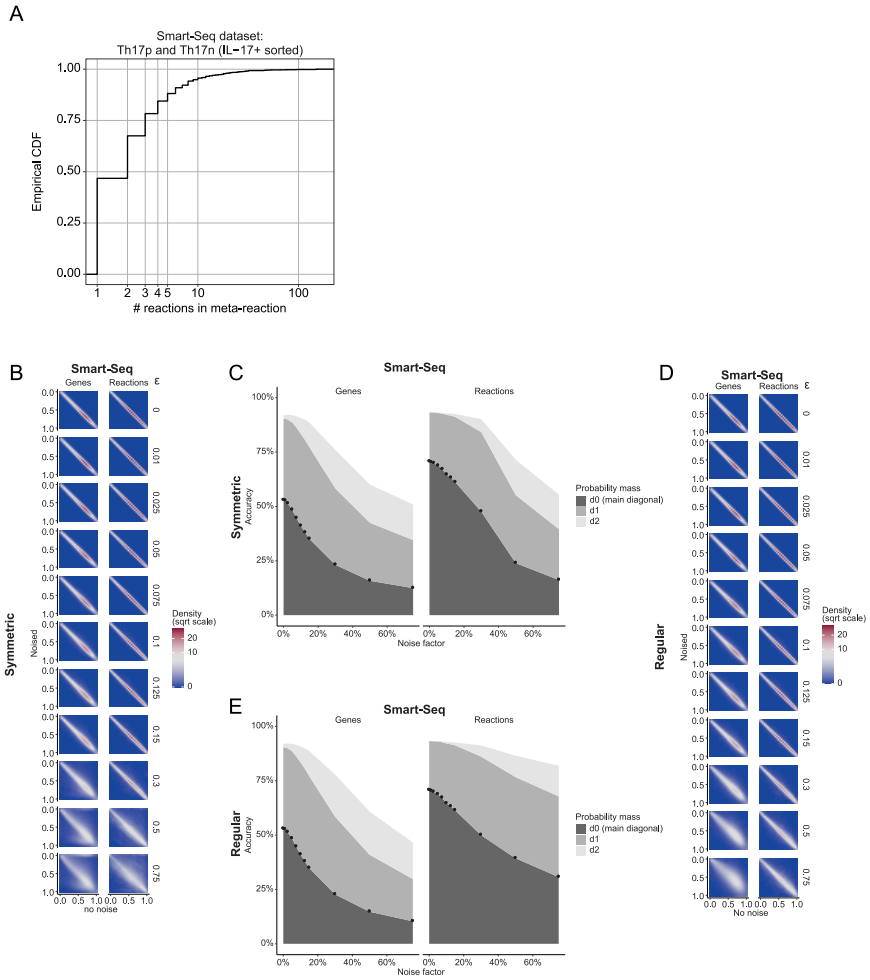

Figure S1. Algorithm overview, related to Figure 1

(A) Cumulative distribution function (CDF) of number of reactions per meta-reaction. (B-C) Random noise ε was added to the input gene expression matrix with two transcription noise models ("symmetric" and "regular") as described in the STAR Methods. (B) Left column: expression for every gene was scaled to [0,1] range. Two-dimensional density was computed over the of original and noised expression per gene is shown; right column: similarly, compass scores for every reaction were scaled to [0,1] and 2d density for raw and noised scores is shown. (C) Total probability mass under the 2d density surface was computed for (d0) the main diagonal; (d1) the two diagonals above and below the main diagonal; (d2) similarly, the two diagonals above and below the d1 diagonals.

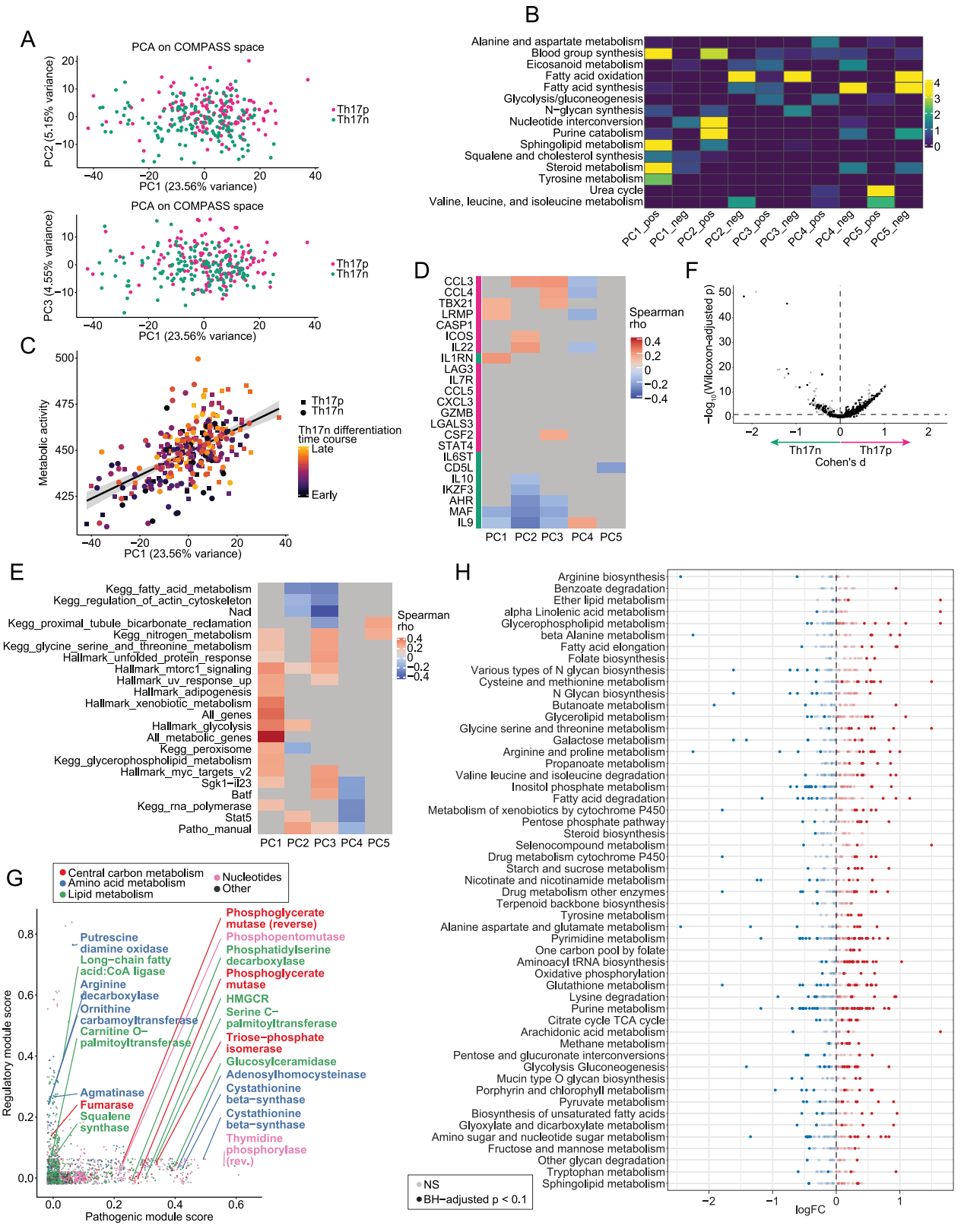

(legend on next page)

Figure S2. Compass-based exploration of metabolic heterogeneity within the Th17 compartment, related to Figure 2

(A-E) PCA of Compass space restricted to core meta-reactions, see main text. (A) PC1 scores plotted against PC2 and PC3 scores. (B) Enrichment of metabolic pathways in the positive or negative directions of top principal components. Enrichment is computed with GSEA (Subramanian et al., 2005) over single reactions (rather than genes, as in the common applications). Colors are -log10(BH-adjusted p), truncated at 4, with p being the GSEA p value. Pathways correspond to Recon2 subsystems. (C) PC1 scores plotted against computational signatures of cellular metabolic activity and Th17 differentiation time course (STAR Methods). (D) Spearman correlation of top PCs with known pro-pathogenic (magenta) and pro-regulatory (green) marker genes, none of which is metabolic. Only significant correlations (BH-adjusted $p < 0.1$) are shown in color. (E) Spearman correlation of computational transcriptome signatures with the top principal components. Only significant correlations (BH-adjusted $p < 0.1$) are shown in color and non-significant correlation coefficients are greyed out. See STAR Methods for signature computation. (F) Same analysis as shown in Figure 2C, but showing all reactions (and not just ones belonging to certain pathways, as in the main figure). (G) We computed a pro-pathogenic score for each reaction by taking the ratio of pro-pathogenic and pro-regulatory markers with which it correlates and anti-correlates, respectively (BH-adjusted $p < 0.1$ for a Spearman correlation) out of the 23 marker genes (listed in Figure 2D and STAR Methods). Similarly, we computed pro-regulatory reaction scores. Only core reactions are shown. (H) Same analysis as shown in Figure 2E, only at the gene expression level (and not reaction level based on Compass scores). Genes are grouped by KEGG pathways (and may be annotated as belonging to more than one pathway).

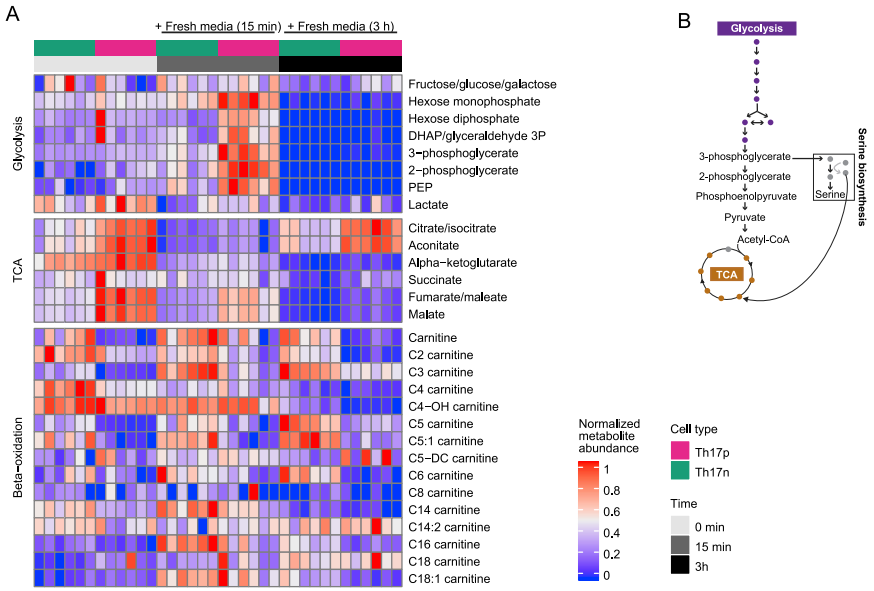

Figure S3. Differential usage of glycolysis and fatty acid oxidation by pathogenic and non-pathogenic Th17 cells, related to Figure 3

(A) Parallel of main Figures 3C showing also 3h after fresh media pulse. (B) The glycolysis pathway, as shown in main Figure 4A, highlighting its junction with serine biosynthesis.

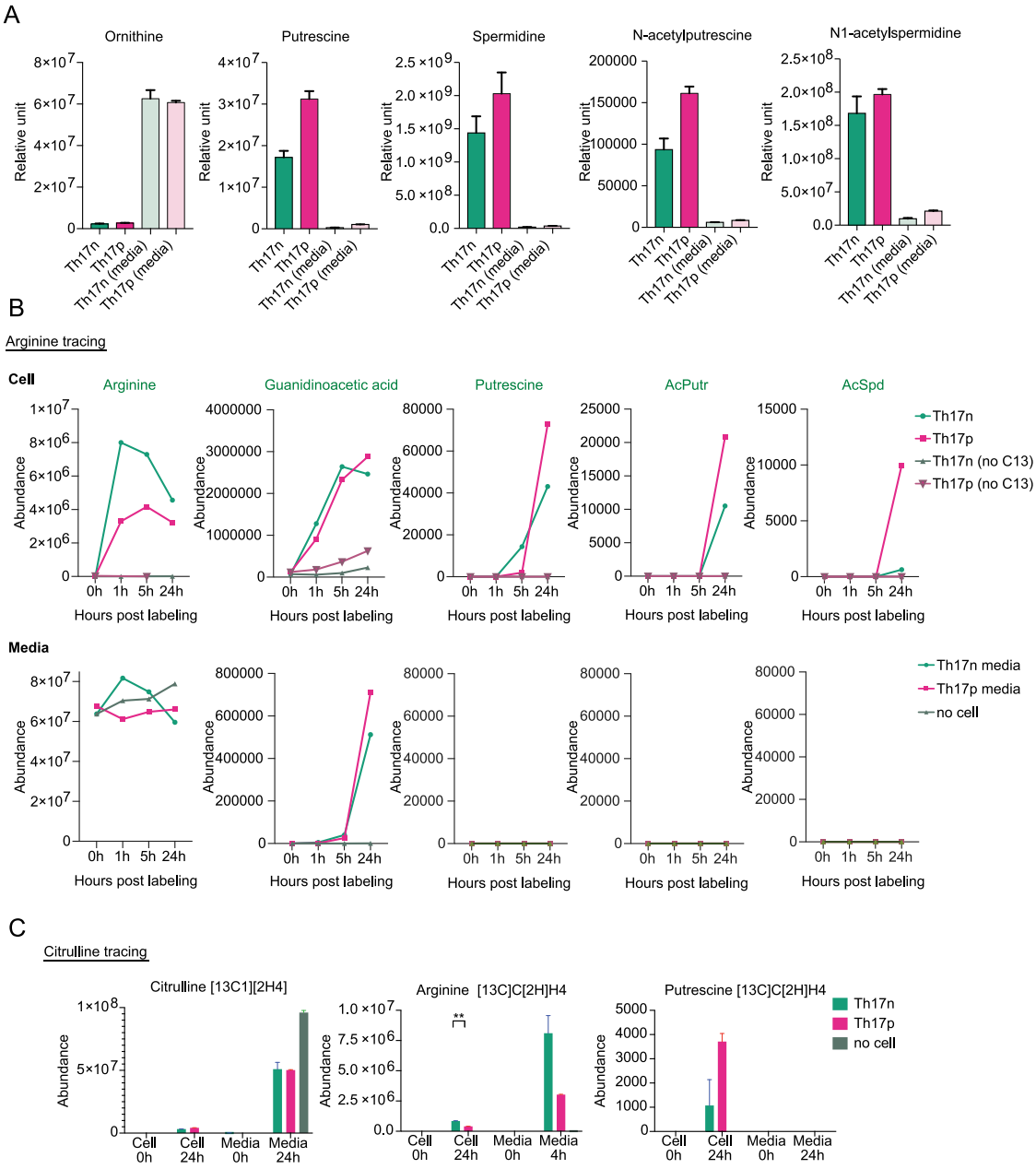

Figure S4. Prediction and metabolic validation of the polyamine pathway as a candidate in regulating Th17 cell function, related to Figure 4

(A) Metabolomics analysis of the polyamine pathway as in Figure 1H. Cell lysates as well as media from Th17n and Th17p differentiation cultures are shown. (B-C) Carbon tracing in the polyamine pathway. Th17n and Th17p cells were differentiated as described (STAR Methods), lifted to rest at 68 hours and pulsed with C13 labeled Arginine (B) or Citrulline (C) followed by LC/MS analysis at time points indicated.

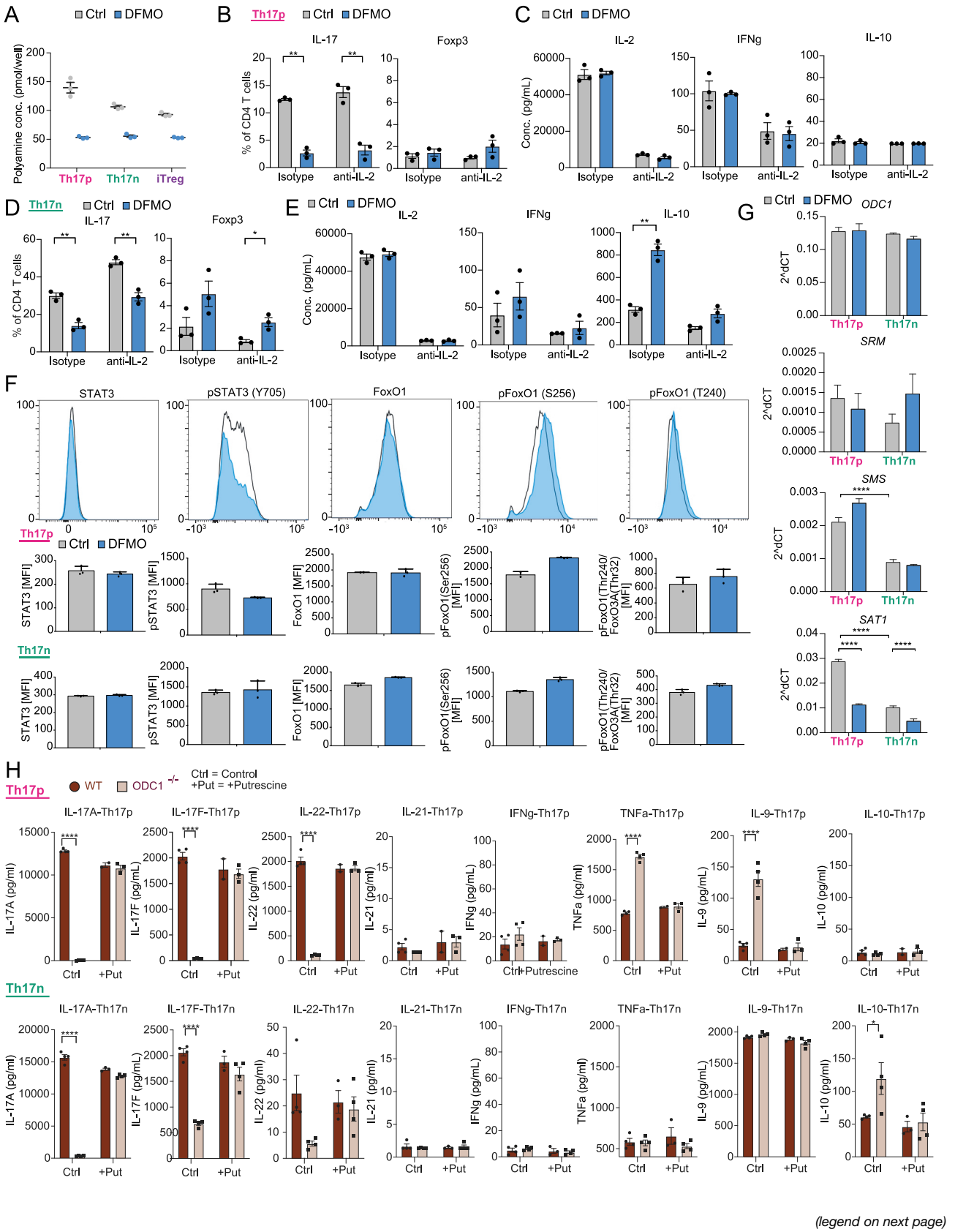

(legend on next page)

Figure S5. Chemical and genetic interference with the polyamine pathway suppress canonical Th17 cell cytokines, related to Figure 5

(A) The effect of DFMO on cellular polyamine concentration is measured by an enzymatic assay. Th17p, Th17n and iTregs are differentiated in the presence of DFMO and harvested at 96 hours for analysis. (B-E) IL-2 neutralization does not regulate the effect of ODC1 inhibition. 10ug/ml of anti-IL-2 antibody or isotype control were added at the time of Th17n or Th17p cell differentiation with control or DFMO. Cells were analyzed by B,D, flow cytometry and C,E, supernatant were analyzed for cytokine secretion. Welch t test significance is denoted. (F) Protein and phospho-protein analysis by flow cytometry for Th17n and Th17p cells treated with control of DFMO. (G) The effect of DFMO on enzymes in the polyamine pathway as measured by qPCR. Th17p and Th17n cells were differentiated in the presence of control or DFMO and harvested at 48h for RNA extraction and qPCR analysis. (H) The effect of genetic perturbation of ODC1 on cytokine production from Th17p (upper panels) and Th17n cells (lower panels). Supernatant from Th17p and Th17n differentiation culture was harvested at 96 hours and analyzed by legendplex for cytokine concentration.

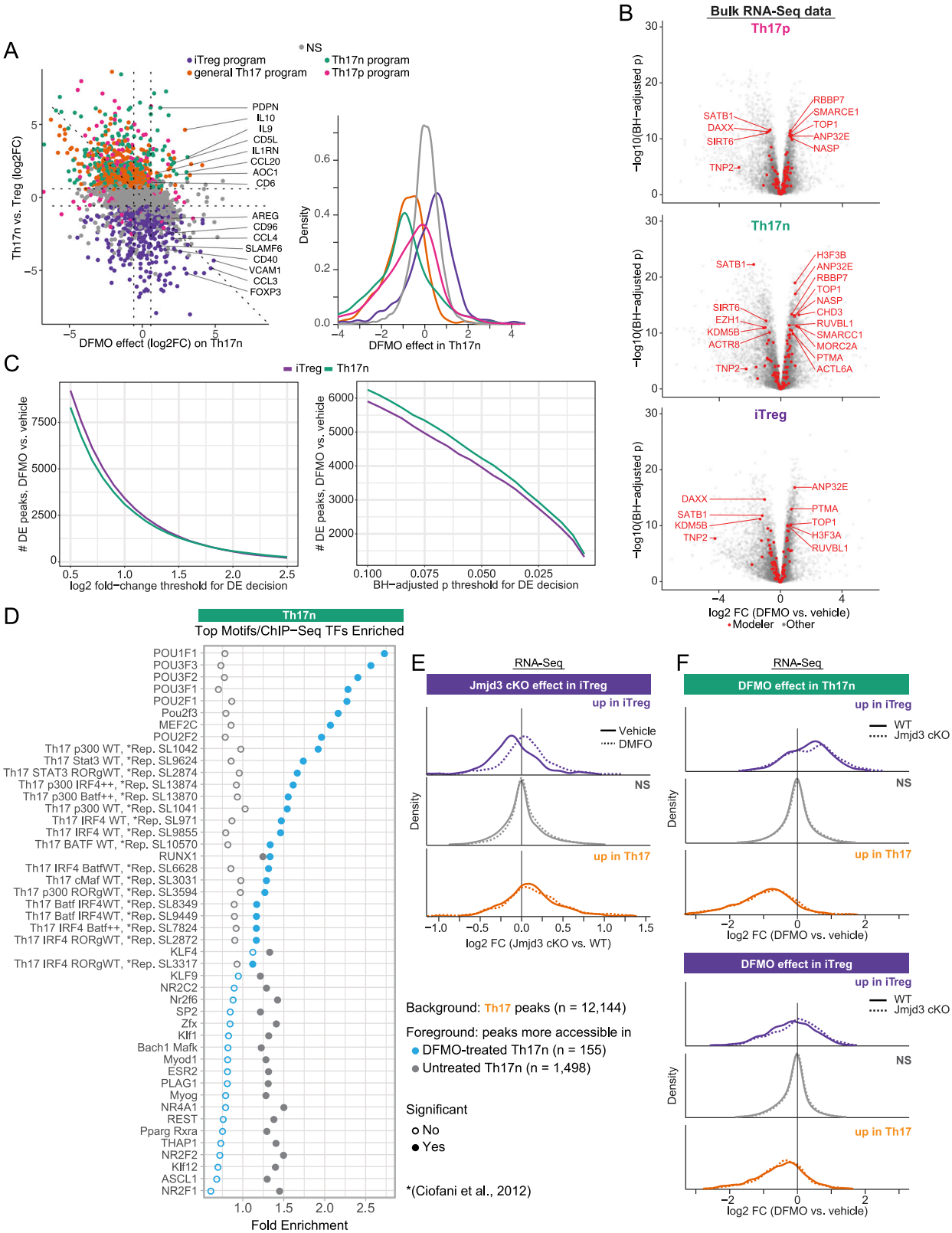

(legend on next page)

Figure S6. DFMO treatment promotes Treg-like transcriptome and epigenome, related to Figure 6

(A) Log2 fold changes for a comparison between DFMO-treated and vehicle-treated Th17n cells (x axis), and Th17n versus iTreg cells (both vehicle-treated; y axis) are based on the same data described in manuscript Figures 6A–6C. Dots represent genes, which are divided into 5 groups based on differential expression in untreated cells (STAR Methods). Dashed lines correspond to the logFC threshold used in differential expression calling log2(1.5) (STAR Methods). Differentially expressed genes by either of the comparisons shown in the axes are opaque and transparent otherwise. (B) Volcano plots showing affected chromatin modifiers by DFMO treatment in Th17n, Th17p and iTreg cells. (C) Number of differentially expressed (DE) peaks between DFMO and vehicle-treated cells as a function of the significance threshold. Upper panel, log2FC used as threshold; Lower panel, BH-adjusted P used as threshold. (D) Similar analysis to Figure 6F, only using Th17 background instead of Treg. I.e., dots represent fold enrichment of peaks more accessible in DFMO-treated (blue) or untreated (gray) Th17n cells against a background of Th17 peaks as described in the manuscript (i.e., this analysis considers only peaks that were differentially more accessible in untreated Th17 compared to untreated iTreg, corresponding to the orange curve in Figure 6D). (E-F) Cells were cultured under Th17n or iTreg condition with DFMO or solvent control (water) as in Figure 6 and harvested at 68h for RNA-Seq. Treg and Th17 programs were defined as in Figure 6H (STAR Methods). E, Histogram showing the effects of JMJD3 conditional knockout (cKO) in control versus DFMO-treated Treg cells. F, Histogram showing the effects of DFMO in WT versus $JMJD3^{fl/fl}CD4^{cre}$ in Th17n and Treg cells.

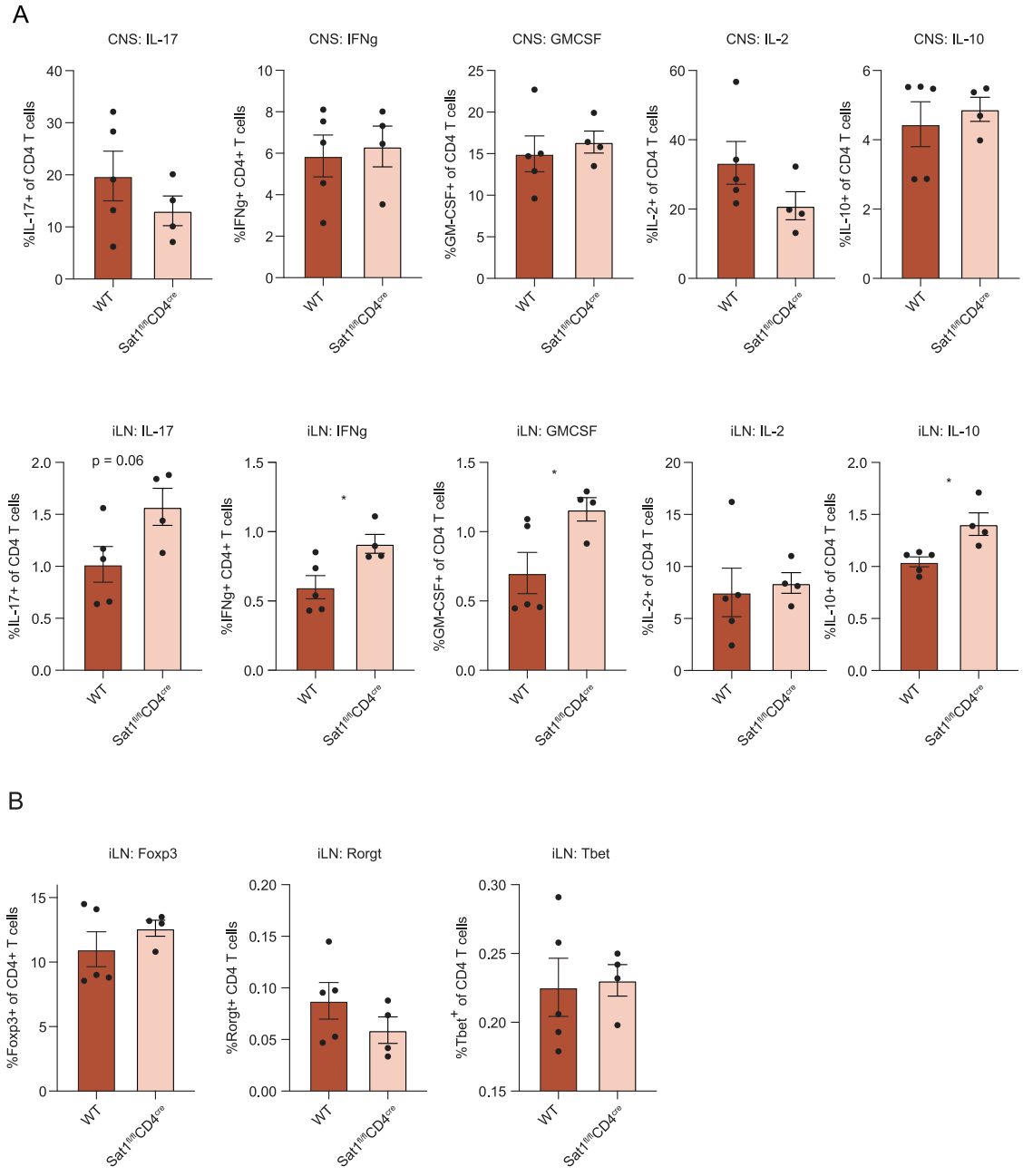

Figure S7. Targeting ODC1 and SAT1 alleviate EAE, related to Figure 7

Cells were isolated from CNS or inguinal lymph node (iLN) of WT or SAT1$^{fl/fl}$CD4^{cre} mice on day 15 post EAE induction (similar experiments as in Figure 4F). (A) Intracellular cytokines were measured by flow cytometry after 4-hour PMA/ionomycine stimulation *ex vivo* in the presence of brefaldin and monensin. (B) Transcription factors were analyzed directly *ex vivo* by intracellular staining.